

# We are IntechOpen, the world's leading publisher of Open Access books Built by scientists, for scientists

6,900

Open access books available

186,000

International authors and editors

200M

Downloads

Our authors are among the

154

Countries delivered to

TOP 1%

most cited scientists

12.2%

Contributors from top 500 universities



WEB OF SCIENCE™

Selection of our books indexed in the Book Citation Index  
in Web of Science™ Core Collection (BKCI)

Interested in publishing with us?  
Contact [book.department@intechopen.com](mailto:book.department@intechopen.com)

Numbers displayed above are based on latest data collected.  
For more information visit [www.intechopen.com](http://www.intechopen.com)



# Dramatic Weakening and Embrittlement of Intact Hard Rocks in the Earth's Crust at Seismic Depths as a Cause of Shallow Earthquakes

*Boris Tarasov*

## Abstract

Frictional stick-slip instability on pre-existing faults is well studied experimentally and considered as the general mechanism for shallow earthquakes. At the same time, post-peak properties of intact hard rocks under high confining stresses  $\sigma_3$  corresponding to seismic depths of shallow earthquakes are still unexplored experimentally due to uncontrollable and violent failure of rock specimens even on modern stiff and servocontrolled testing machines. The lack of knowledge about post-peak properties of the majority of the earthquake host rocks prevents us from understanding and quantifying the contribution of these rocks to shallow earthquakes. This paper discusses a recently identified shear rupture mechanism operating in hard rocks under high  $\sigma_3$  which causes dramatic rock weakening and embrittlement (by tenths of times) during the post-peak failure. The unknown before 'abnormal' properties of hard rocks imply the fundamentally different general mechanisms for shallow earthquakes. It is shown that in the earth's crust, the new mechanism acts in the vicinity of pre-existing faults only and provides the formation of new dynamic faults in intact rocks at very low shear stresses (significantly less than the frictional strength). The fault propagation is characterised by extremely low rupture energy and small stress drop. These 'abnormal' properties make hard rocks the main and more dangerous source of shallow earthquakes in comparison with pre-existing faults.

**Keywords:** extreme shear ruptures, shear rupture mechanism, hard rocks, shallow earthquakes, rock weakening and embrittlement

## 1. Introduction

Today, frictional stick-slip instability on pre-existing faults is considered as the general mechanism of shallow earthquakes. This concept is based on a number of features observed for natural and laboratory earthquakes which support the stick-slip nature of earthquakes as opposed to failure of intact rocks. Some of these features are: nucleation of earthquakes at tectonic plate boundaries and other pre-existing faults, recurring stick-slip instability along a pre-existing fault, low shear

stresses activating earthquakes, small stress drop and specific depth-frequency distribution of earthquake hypocentres with a maximum at a special depth [1–9].

The nature of friction and stick-slip instability for rocks in association with earthquakes has been comprehensively studied during the last half of a century [1, 5, 7, 10–15]. At the same time, post-peak properties of intact hard rocks under high confining stresses  $\sigma_3$  corresponding to seismic depths of shallow earthquakes are still unexplored experimentally. The reason for that is uncontrollable and violent failure of rock specimens even on modern stiff and servocontrolled testing machines. Today, post-peak properties of hard rocks at high  $\sigma_3$  and the failure mechanism operating at these conditions are treated by analogy with conventional understanding based on experimental results obtained for softer rocks. The paper shows that this analogy is unacceptable because the real properties of hard rocks at high  $\sigma_3$  differ fundamentally from the conventional understanding. The lack of knowledge about post-peak properties of the majority of the earthquake host rocks prevents us from understanding and quantifying the contribution of these rocks to shallow earthquakes.

The paper discusses a recently identified shear rupture mechanism operating in hard rocks under high  $\sigma_3$  that is responsible for extreme rupture dynamics [16–23]. The mechanism was identified on the basis of comprehensive analysis of side effects accompanying extreme ruptures. The new mechanism provides two remarkable features in the rupture head: (1) low shear resistance approaching zero and (2) highly amplified shear stresses. The combination of these features allows for a shear rupture to propagate through intact rock spontaneously at very low shear stresses applied with the absorption of a small amount of energy which indicates dramatic rock weakening and embrittlement at high  $\sigma_3$ . Due to the weakening and embrittlement during the failure process, the stress-strain curves for laboratory specimens look very specific in the post-peak region indicating ‘abnormal’ properties.

The paper demonstrates that in the earth’s crust, the new mechanism is active in the vicinity of pre-existing faults only and can provide the formation of new dynamic faults in intact rocks at very low shear stresses (up to an order of magnitude less than the frictional strength). The fault propagation is accompanied by extremely low rupture energy and small stress drop which can be smaller than for stick-slip instability on pre-existing faults. It is shown that some earthquake features currently attributed to the stick-slip instability on pre-existing faults can be provided by the new mechanism for ruptures propagating in intact rocks. Some of these features are nucleation on the basis of pre-existing faults, recurring instability on a pre-existing fault, activation of earthquakes at low shear stresses, small stress drop and specific depth-frequency distribution of hypocentres.

The unknown before ‘abnormal’ properties of hard rocks at high  $\sigma_3$  make intact rocks more dangerous in respect of shallow earthquakes than pre-existing faults because the new mechanism can generate dynamic faults at shear stresses significantly below the frictional strength. The proximity of the pre-existing fault to the zone of dynamic new fracture development in intact rock creates the illusion of frictional stick-slip instability on the pre-existing fault, thus concealing the real situation. According to the new knowledge, intact hard rocks adjoining pre-existing faults represent the general source of shallow earthquakes.

## 2. Post-peak properties of hard rocks at high $\sigma_3$ : conventional and new understanding

**Figure 1** illustrates the situation with our current knowledge about rock properties beyond the peak stress at triaxial compression of type  $\sigma_1 > \sigma_2 = \sigma_3$ . Such

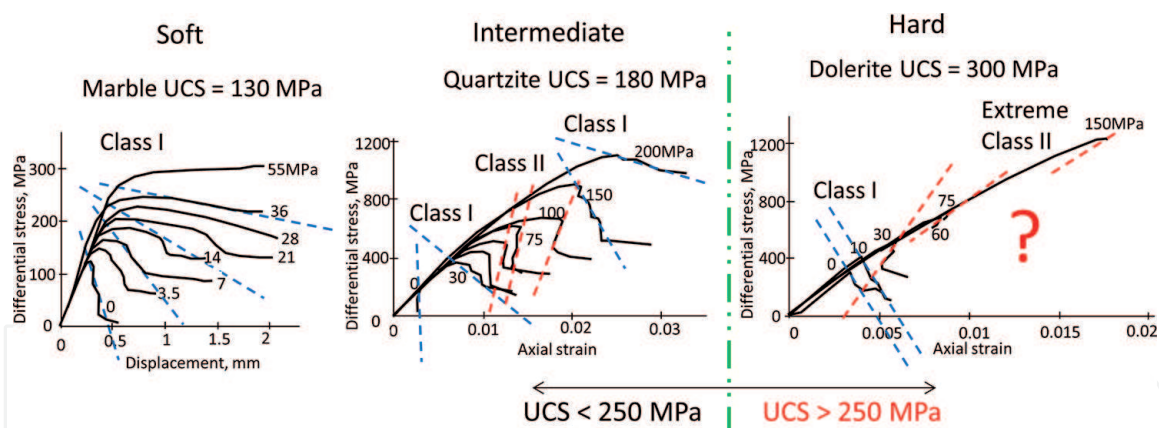


**Figure 1.**  
 Three sets of stress-strain (displacement) curves illustrating features of post-peak behaviour for soft, intermediate and hard rocks.

stress conditions are normally used in laboratory experiments to simulate on rock specimens stress conditions typical for the earth's crust at different depths. **Figure 1** shows three sets of stress-displacement curves obtained at different levels of confining stress  $\sigma_3$  for rocks of different hardness. Rock hardness here is characterised by uniaxial compressive strength (UCS) and increases from left to right. The curves demonstrate how rock hardness affects post-peak behaviour at rising  $\sigma_3$ . Relatively soft rocks on the left (represented by marble with UCS = 130 MPa [24]) exhibit class I behaviour at all levels of  $\sigma_3$  (indicated by blue dotted lines) and show an increase in post-peak ductility with rising  $\sigma_3$ . Rocks of intermediate hardness (represented by quartzite with UCS = 180 MPa) exhibit post-peak embrittlement within a certain range of  $\sigma_3$  which is expressed by transition from class I to class II behaviour (indicated by red dotted lines). At lower and higher  $\sigma_3$ , the post-peak ductility increases with rising  $\sigma_3$ .

The typical behaviour of hard rocks (represented by dolerite with UCS = 300 MPa) is characterised by dramatic embrittlement at high  $\sigma_3$  leading to extreme class II behaviour. It is important to note that the transition from class I to class II for this rock occurs at  $\sigma_3 = 30$  MPa. At relatively low  $\sigma_3$ , the post-peak failure can be controlled both for class I and class II on stiff and servocontrolled testing machines. However, at  $\sigma_3 > 50$  MPa, the failure process associated with propagation of a shear rupture becomes uncontrollable and abnormally violent. With rising  $\sigma_3$  rock brittleness and the violence increase. However, we can suppose that at very high  $\sigma_3$ , by analogy with intermediate rocks, hard rocks should also return to more ductile behaviour. Hard rocks with similar post-peak behaviour are represented mainly by volcanic and highly metamorphic rocks with UCS > 250 MPa.

**Figure 1** demonstrates that the effect of embrittlement within a certain range of high  $\sigma_3$  (different for different rocks) increases with increasing rock hardness. The problem is that all existing ultra-stiff servocontrolled testing machines cannot provide controllable failure for hard rocks at high  $\sigma_3$  corresponding to stress conditions of seismic depth for shallow earthquakes. Due to this limitation in testing capability, post-peak properties of hard rocks at high  $\sigma_3$  are experimentally unexplored. Today, post-peak properties of hard rocks at high  $\sigma_3$  and the failure mechanism operating at these conditions are treated by analogy with conventional understanding based on experimental results obtained for softer rocks.

On the basis of comprehensive analysis of side effects accompanying extreme ruptures, an unknown before shear rupture mechanism and inaccessible post-peak properties of hard rocks generated by this mechanism were recently identified [16–23]. In this section we will demonstrate only the fundamental difference



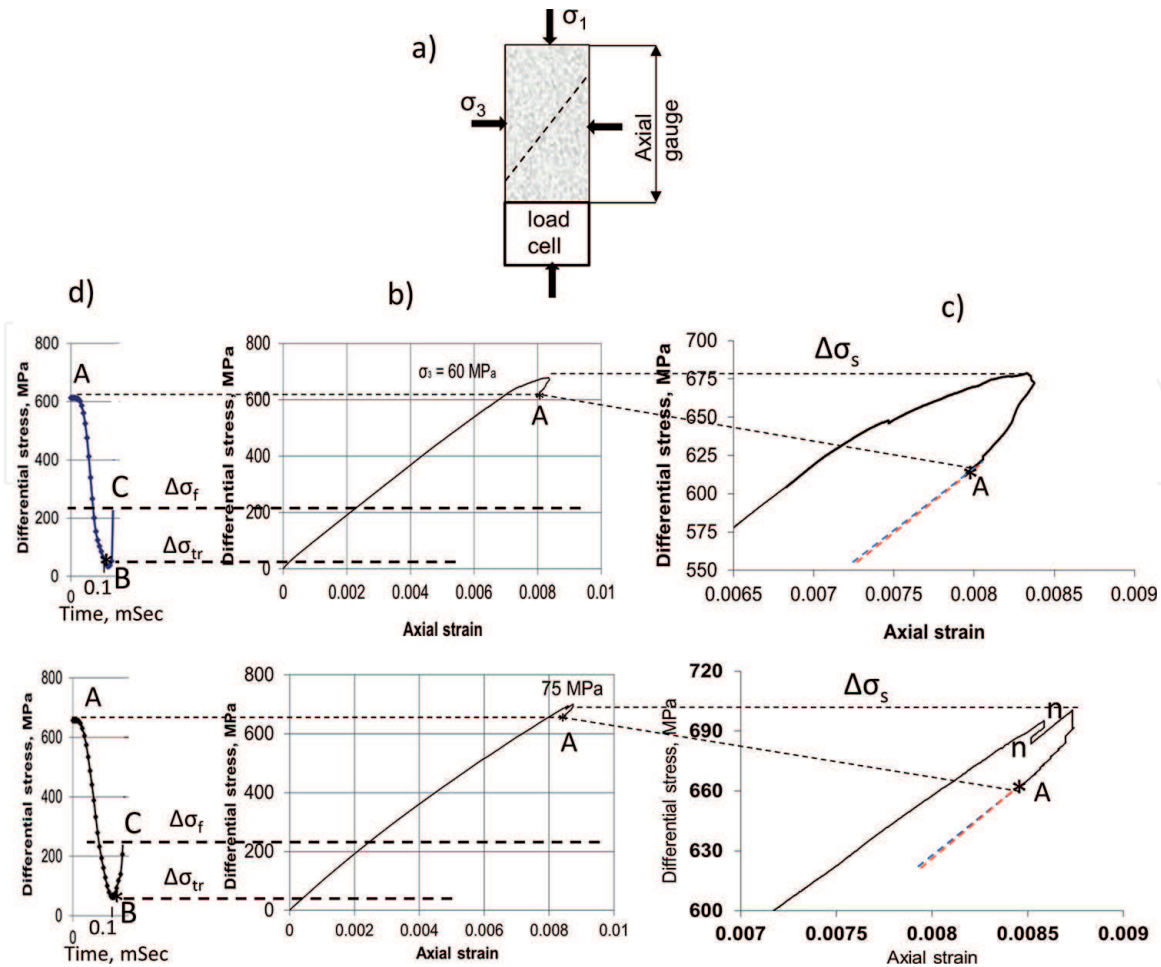


**Figure 2.**

*Some typical features of post-peak behaviour of hard rocks at highly confined compression illustrated by experimental results obtained for dolerite specimens at  $\sigma_3 = 60 \text{ MPa}$  and  $\sigma_3 = 75 \text{ MPa}$ .*

between the conventional and new understanding of post-peak properties of hard rocks at high  $\sigma_3$ . The new failure mechanism and more detailed information about hard rock behaviour in laboratory and natural conditions will be discussed in the following sections of the paper.

**Figure 2** demonstrates some features typical for post-peak behaviour of hard rocks at high  $\sigma_3$ . It shows experimental results obtained for dolerite specimens with UCS = 300 MPa tested under  $\sigma_3 = 60 \text{ MPa}$  and  $\sigma_3 = 75 \text{ MPa}$ . **Figure 2a** illustrates schematically a cylindrical specimen equipped with an axial gauge and a load cell as used in experiments. The failure process at high  $\sigma_3$  is always associated with a shear rupture propagation shown by a dotted line on the specimen body. **Figure 2b** shows two stress-strain curves where points A indicate the final stage of controllable post-peak failure after which the spontaneous and violent shear rupture propagation took place. **Figure 2c** shows enlarged fragments of the stress-strain curves involving the post-peak stage. The post-peak curves here reflecting real rock properties up to point A were easily obtained in static regime due to controllable reverse deformation of the specimen provided by the servo-controlled system. However, beyond point A, the failure control became impossible. The reason for that is as follows. At point A, the post-peak modulus (represented by a red line on the graphs) became practically equal to the unloading elastic modulus (represented by a blue line on the graphs) which corresponds to the extreme Class II behaviour. The unloading modulus was determined by unloading the specimen tested under  $\sigma_3 = 75 \text{ MPa}$  at the peak stress (marked as n-n on the graph). The fact that the post-peak modulus and unloading modulus are practically coincide indicates that the post-peak rupture energy beyond points

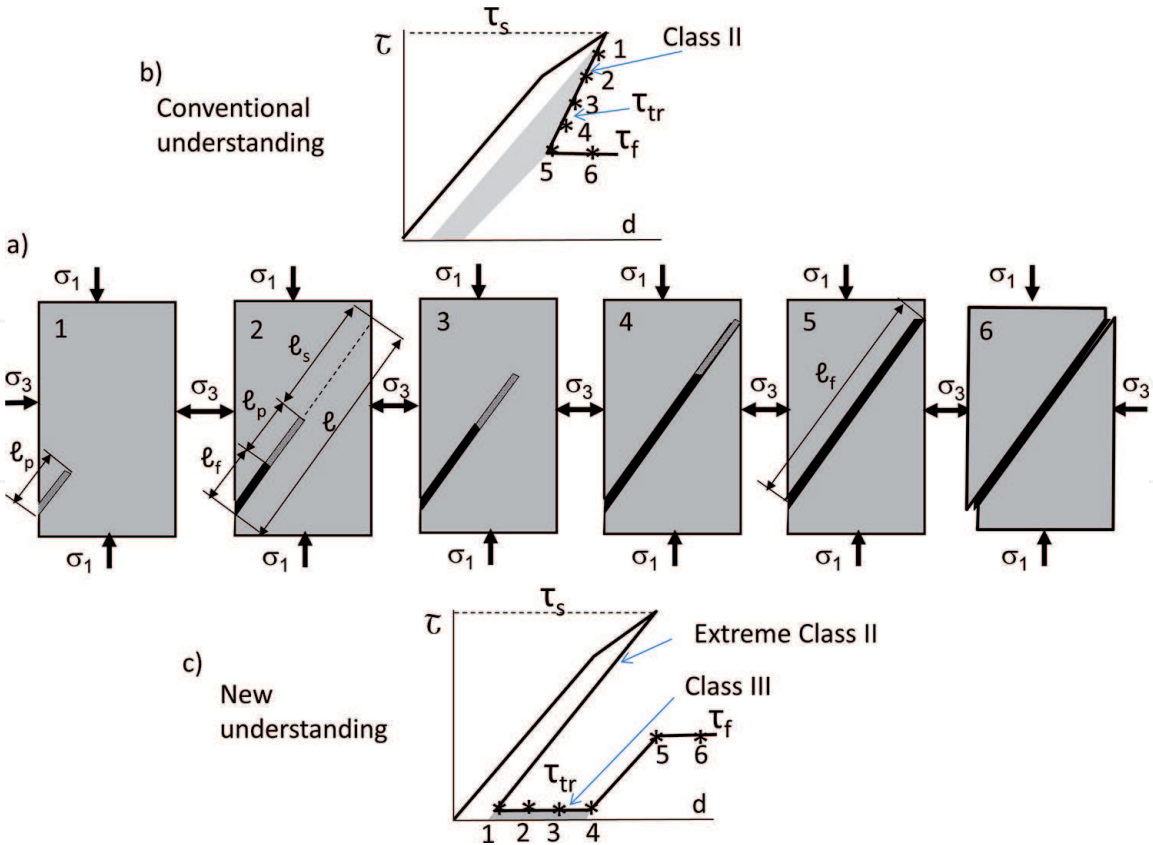


**Figure 3.** Schematic illustration of the fundamental difference between the conventional and the new understanding of post-peak properties of hard rocks tested at high  $\sigma_3$ .

A is vanishingly small. The controllable failure at this situation becomes impossible because the existing testing machines are unable to provide sufficiently fast specimen unloading to stop the rupture propagation. The spontaneous failure at high  $\sigma_3$  is usually abnormally violent and accompanied by strong sound and shudder of the testing machine.

Because during the spontaneous failure the testing machine cannot provide sufficiently fast unloading of the specimen to follow the actual post-peak modulus, the readings of gauges obtained at this stage of failure do not reflect the actual post-peak properties of the failing specimen. At the same time, the conducted above analysis of the post-peak modulus at point A allows supposing that the stress-strain curve beyond point A should be very close (practically coincide) to the unloading elastic curve. Another very important post-peak feature typical for hard rocks at high  $\sigma_3$  can be observed on the stress-time curves recorded by the load cell in **Figure 2d**. These curves demonstrate that during the spontaneous failure the specimen strength at a certain stage becomes significantly below the static frictional strength, the level of which is represented by a horizontal dotted line  $\Delta\sigma_f$ . The static frictional strength was determined experimentally by deforming the failed specimen at low strain rates. The least level of the specimen transient strength during the spontaneous failure corresponding to point B is indicated by a horizontal dotted line  $\Delta\sigma_{tr}$  that is about 10 times less than the static frictional strength  $\Delta\sigma_f$ . It will be shown later that the observed in these experiments the extreme Class II behaviour and the abnormally low specimen transient strength are provided by the new shear rupture mechanism.

Using the obtained results, we can formulate a hypothesis about the fundamental difference in post-peak properties of hard rocks at high  $\sigma_3$  in terms of the conventional and the new understanding illustrated in **Figure 3**. **Figure 3a** shows

six stages of shear rupture propagation through a specimen. The rupture incorporates a process zone  $\ell_p$  representing the rupture head and a frictional zone  $\ell_f$  located behind the head. In intact zone  $\ell_s$ , located in front of the process zone, shear resistance corresponds to the intact material strength  $\tau_s$ , while behind the process zone (in zone  $\ell_f$ ), shear resistance is equal to the frictional strength  $\tau_f$ . After completion of the process zone at stage 1, the length of  $\ell_p$  stays constant, while the length of the frictional zone  $\ell_f$  increases during the rupture propagation.

In accordance with conventional understanding, the specimen strength beyond the peak stress (transient strength  $\tau_{tr}$ ) at any failure stage is determined roughly by the sum of shear resistance of all three zones along the propagating rupture (intact, process and frictional):

$$\tau_{tr} = \tau_s \frac{\ell_s}{l} + \tau_p \frac{\ell_p}{l} + \tau_f \frac{\ell_f}{l} \quad (1)$$

Shear resistance of the process zone here can be determined roughly as  $\tau_p = (\tau_s + \tau_f)/2$ .

**Figure 3b** illustrates the conventional understanding of post-peak properties of hard rocks at high  $\sigma_3$ . Points on the graph indicate six identical failure stages shown for the specimen in **Figure 3a**. The specimen strength at each stage is described by Eq. (1). Here, during the failure process, the transient strength decreases gradually by substituting the material strength with frictional strength. At stages 5 and 6, the specimen strength is determined by friction in the fault which is considered today to be the lower limit on rock shear strength. The post-peak rupture energy between stages 1 and 5 corresponds to the shaded area under the curve.

**Figure 3c** illustrates the new understanding of post-peak properties of hard rocks at high  $\sigma_3$ . It will be shown later that the new mechanism provides very low shear resistance of the completed process zone which can be  $\tau_p \approx 0.1\tau_f$ . Furthermore, the new mechanism represents a very powerful stress amplifier (based on an unknown before principle) providing high shear stresses in the process zone at low shear stresses applied. These two unique features after completion of the process zone at stage 1 make it possible for the shear rupture to propagate through intact rock even at very low shear stresses applied  $\tau$  which can be significantly (up to an order of magnitude) less than the frictional strength. In this case the specimen transient strength at controllable failure is determined solely by the process zone strength:  $\tau_{tr} = \tau_p$ .

**Figure 3c** shows that controllable failure can be provided if the testing machine is capable to unload the specimen up to the level  $\tau_{tr} = \tau_p$  at the moment of completion of the process zone (stage 1). The extreme Class II stage beyond the peak stress is associated with the initial formation of the process zone. After that the rupture can propagate statically through the specimen at applied stresses slightly above  $\tau_{tr} = \tau_p$  which represents the specimen strength between failure stages 1 and 4. The rupture propagation through intact rock at a constant shear stress significantly below the frictional strength we will classify as Class III. The post-peak rupture energy between stages 1 and 4 corresponds to the shaded area on the graph. This very low energy absorption implies very high brittleness of the material at the failure process. After stage 5 when the process zone has crossed the specimen, the situation changes. The specimen strength at stages 5 and 6 is determined by friction in the developed fault. To provide displacement along the developed fault, it is necessary to increase the applied stress up to  $\tau_f$ .

It should be noted that if the testing machine cannot provide sufficiently fast unloading at the moment of completion of the process zone (stage 1), the failure process will be spontaneous and violent because in this case the applied stress



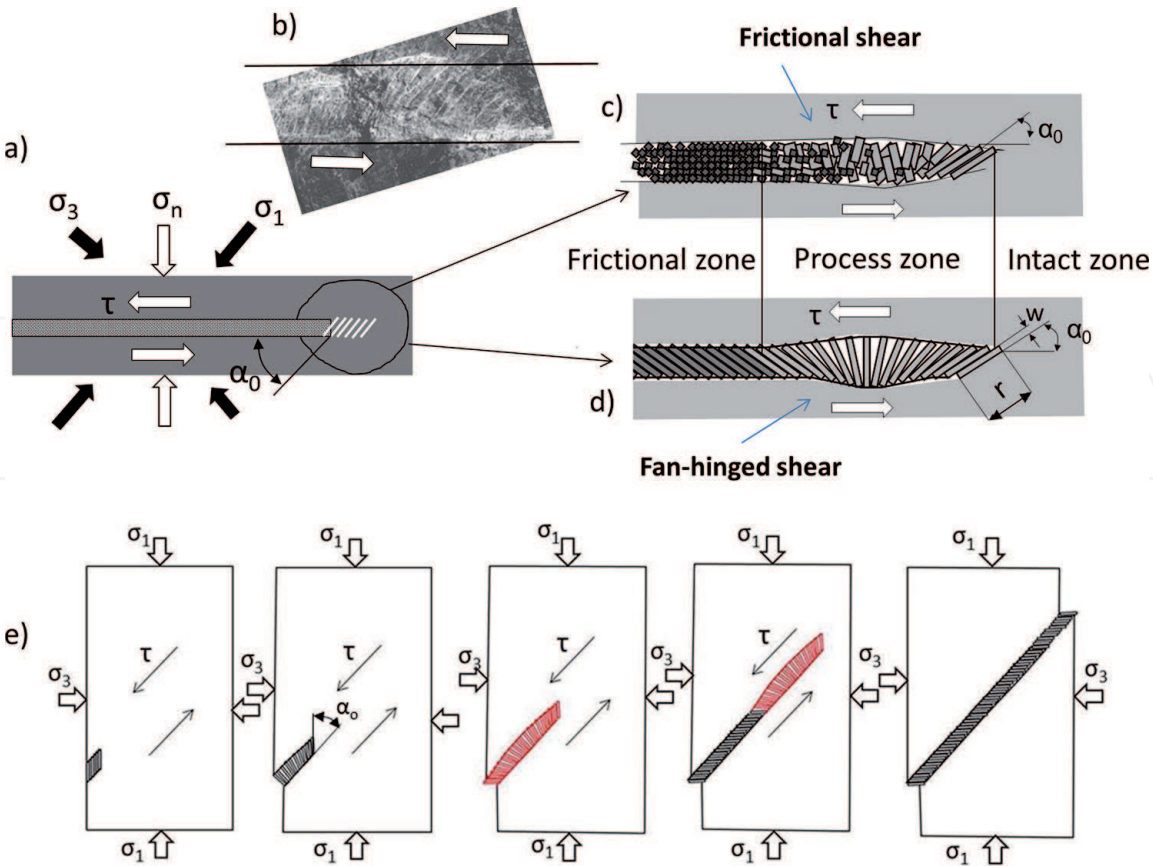


**Figure 4.** a) and b) Nature of shear rupture growth in hard rocks at high  $\sigma_3$ , c) and d) The difference between the conventional (frictional) and the new (fan-hinged) shear rupture mechanisms. e) Illustration of the fan-structure formation and propagation through a rock specimen.

exceeds the material strength which corresponds to  $\tau_{tr} = \tau_p$ . It is important to note also that in the case of spontaneous failure, the load cell adjoining the specimen (see **Figure 3a**) will record the variation of stresses applied to the specimen from the testing machine but not the actual material strength determined by the process zone. The actual strength of the process zone can be reflected by the load cell when the applied stress decreases to the level  $\tau_{tr} = \tau_p$  which corresponds to point B in **Figure 2d**. The new shear rupture mechanism that is responsible for the discussed ‘abnormal’ post-peak properties including Class III behaviour of hard rocks under high  $\sigma_3$  will be introduced in the next sections.

### 3. General principles of the new mechanism operating in hard rocks at high $\sigma_3$

#### 3.1 Structure of shear ruptures

**Figure 4** illustrates the nature of shear rupture propagation in brittle intact rocks at high  $\sigma_3$ . In **Figure 4a** a shear rupture propagates from left to right under stresses  $\sigma_1$ ,  $\sigma_3$ ,  $\sigma_n$  and  $\tau$  representing the applied major and minor stresses and the induced normal and shear stresses. Shear ruptures are known to propagate through brittle rocks because of the creation of an echelon of tensile cracks at the rupture tip generated along the major stress that is at angle  $\alpha_0 \approx (30^\circ \div 40^\circ)$  to the shear rupture plane [25–28]. The echelon of inclined tensile cracks and inter-crack slabs forms a typical structure of shear ruptures illustrated by a photograph in **Figure 4b** (modified from [29]). Horizontal lines here indicate the rupture faces. It was observed



that at relative displacement of the rupture faces, inter-crack slabs are subject to rotation [25–28]. We will call hereafter the inter-crack slabs as domino blocks.

**Figure 4c** and **d** show two fundamentally different behaviours of domino blocks at rotation which characterise the conventional and the new understanding of failure mechanisms operating in hard rocks at high  $\sigma_3$ . According to the conventional understanding in **Figure 4c**, domino blocks collapse at rotation creating friction within the process zone in the rupture head [25–28]. This mechanism is associated with frictional shear and provides conventional post-peak properties illustrated in **Figure 3b**. According to the new understanding (**Figure 4d**), domino blocks can withstand the rotation without collapse at a certain combination of such parameters as domino block geometry (ratio between the block length  $r$  and width  $w$ ), rock strength (determining the strength of domino blocks) and applied stresses. Because the relative shear displacement of the rupture faces increases with distance from the rupture tip, the successively generated and rotated domino blocks form a fan-like structure that represents the rupture head [16–23]. This mechanism is associated with fan-hinged shear within the fan zone and with the following two fantastic features of the fan structure: (1) extremely low shear resistance approaching zero and (2) high amplification of shear stresses.

The fan mechanism is responsible for the ‘abnormal’ post-peak properties of rock specimens illustrated in **Figure 3c**. **Figure 4e** shows different stages of the fan-structure formation and propagation on the basis of tensile cracking process in a rock specimen. The orientation of tensile cracks and domino blocks in the propagating rupture tip is along  $\sigma_1$ . However, due to relative displacement (shear) of the rupture faces, the domino blocks behind the tip consistently rotate and form the fan structure. Next sections considering unique features of the fan structure will demonstrate that after completion of the fan structure and up to the moment at which the fan has crossed the specimen body, the specimen strength is very low and corresponds to stages 1–4 in **Figure 3c**.

### 3.2 Physical model of the fan mechanism

The problem is that the direct experimental study of the fan mechanism is impossible today, firstly, because modern stiff and servocontrolled testing machines do not allow stopping the failure process governed by the fan mechanism and, secondly, because the fan structure is a transient phenomenon. The fan structure can be in the stable condition during its initial formation before the instability starts and at the final stage of the rupture termination. However,

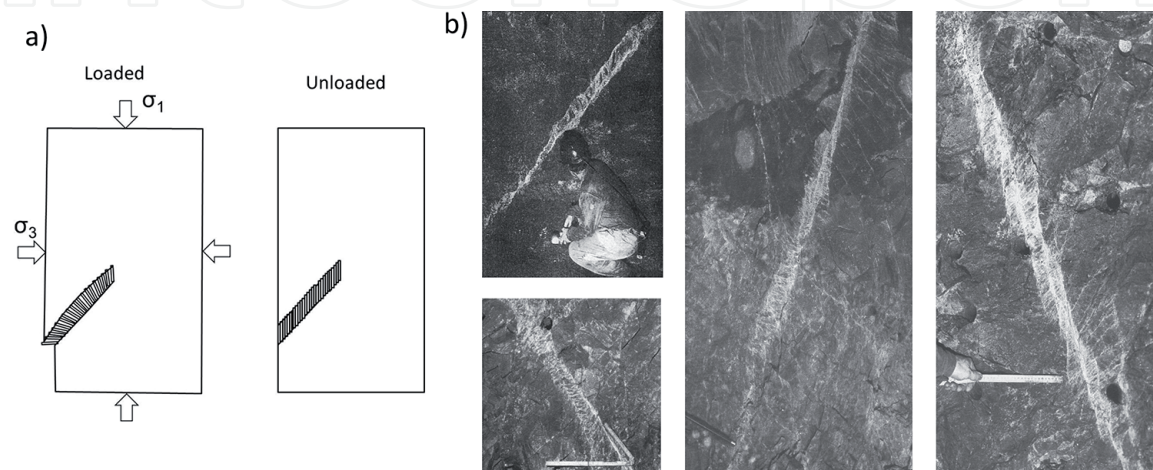


**Figure 5.**  
a) Transient nature of the fan structure and b) the conventional domino-like structure of shear ruptures.

in both cases during total unloading (e.g. associated with the removal of stresses from the specimen or with the tectonic exhumation of the rock mass involving the fan structure), reverse elastic deformations transform the fan into the conventional domino-block structure. **Figure 5a** illustrates this situation schematically on the laboratory specimen. The left specimen shows the fan structure formed during loading. The right specimen demonstrates that during unloading all domino blocks of the fan structure rotate backwards and finally form the conventional domino-like structure that can be seen in natural faults formed in intact rocks (see photographs in **Figure 5b** [29]).

Due to the fact that direct experimental studies of the fan-structure properties are impossible, we will analyse them using a physical model. A video demonstrating the fan-structure formation and propagation along the model can be viewed at [30]. **Figure 6a** shows images of the physical model reflecting different stages of the fan-structure formation and propagation. **Figure 6a-I** shows the initial structure of the future fault that is represented by 'predetermined' domino blocks inclined at an angle  $\alpha_0$  to the rupture plane. All blocks made from tiles are glued together to simulate a 'monolithic' material. The bond strength is less than that of the block material. The row of domino blocks is located between two layers, AB and CD, representing the two opposite faces of the rupture (elastic connectors). The upper and lower faces are fixed to the corresponding ends of each domino block. The entire row of blocks is loaded with an evenly distributed weight,  $\sigma_p$ .

For the physical model, the easiest way to apply shear stress  $\tau$  uniformly distributed along the entire model is the inclination of the model by an angle  $\gamma$ . The distributed weight,  $\sigma_p$  in this case, creates a shear stress  $\tau = \sigma_p \sin(\gamma)$  and normal stress  $\sigma_n = \sigma_p \cos(\gamma)$  along the model. By changing the angle  $\gamma$ , we can vary the applied stresses. Experiments conducted on the physical model show that at angle  $\gamma \approx 80^\circ$ , the upper face AB can move relative to the lower face CD due to the simultaneous separation from each other (tearing off) of all glued together domino blocks with the subsequent rotation of these blocks. We will consider this angle  $\gamma \approx 80^\circ$  as corresponding to the material strength. At the absence of the domino structure, the frictional strength between the upper AB and lower BC faces corresponds to angle  $\gamma = 40^\circ$ .

However, if we form the fan structure from the domino blocks involved in the model, the upper face AB can be moved against the lower face CD at very low angles  $\gamma$  indicating very low shear resistance of the fan structure. Horizontal lines in **Figure 6b** indicate symbolically different levels of shear stresses:  $\tau_s$  corresponds to the material strength,  $\tau_f$  corresponds to the frictional strength,  $\tau_{fan}$  corresponds to the fan-structure strength and  $\tau$  corresponds to a low level of applied shear stress that can cause the fan structure to propagate along the model.

It should be emphasised that for the initial formation of the fan structure, an additional local shear stress should be applied. In the physical model, the initial fan

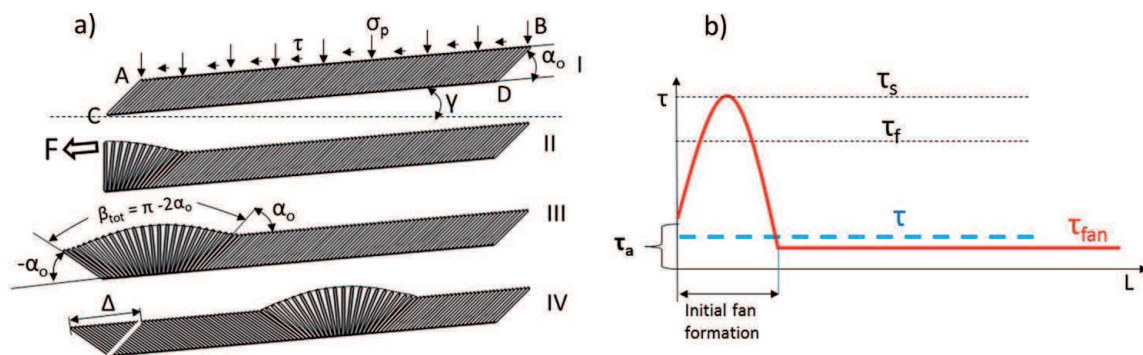


**Figure 6.**  
 Illustration of the physical model of the fan structure.

structure is generated by the application of force  $F$  to the leftmost domino block. When the local stress applied reaches a level  $\tau_a$ , the front block will be torn off from the intact row, indicating the start of the tensile cracking process. The applied force is transmitted to the following blocks by elastically stretching the top rupture face (elastic connector), thereby causing the consecutive separation (tearing off) of the blocks and their rotation against the rupture faces. The fan formation is completed when the first block rotates to a total angle  $\beta_{\text{tot}} = 180^\circ - 2\alpha_0$  at a shear displacement  $\Delta$  of the upper face. The red graph MM in **Figure 6b** reflects the experimentally determined variation in shear resistance of the developing fan structure during its formation and further propagation of the completed fan. The rising resistance up to  $\tau_s$  is associated with the formation of the first half of the fan, while the decreasing resistance corresponds to the second half formation. The reason for such variation in shear resistance will be discussed in the next section.

Experiments on the physical model show that the minimum angle  $\gamma$  at which the fan propagates spontaneously along the model is about  $4^\circ$ . Because the frictional strength for this model is characterised by  $\gamma \approx 40^\circ$ , we can conclude that shear resistance of the fan structure  $\tau_{\text{fan}}$  is by the factor of ten less than the frictional strength:  $\tau_{\text{fan}} \approx 0.1\tau_f$ . It should be emphasised that the low shear resistance takes place within the zone of the moving fan head only. In front of the fan, the material is in an intact condition (strength  $\tau_s$ ). Behind the fan shear resistance is equal to friction (strength  $\tau_f$ ). The fact that the fan structure can propagate through the intact model (representing the ‘intact’ material) at very low shear stresses applied indicates that the material strength in this case is determined by the shear resistance of the fan structure. For the physical model, the fan structure decreases the material strength by the ratio  $\tau_s/\tau_{\text{fan}} \approx 14$ . We can suppose that for the rock specimen in **Figure 2d**, the fan mechanism decreases the material strength at the post-peak failure by the ratio  $\Delta\sigma_s/\Delta\sigma_{\text{tr}} \approx 30$ . The part of the post-peak curve in **Figure 3c** corresponding to the fan propagation through the intact rock specimen is represented by the horizontal line between stages 1 and 4.

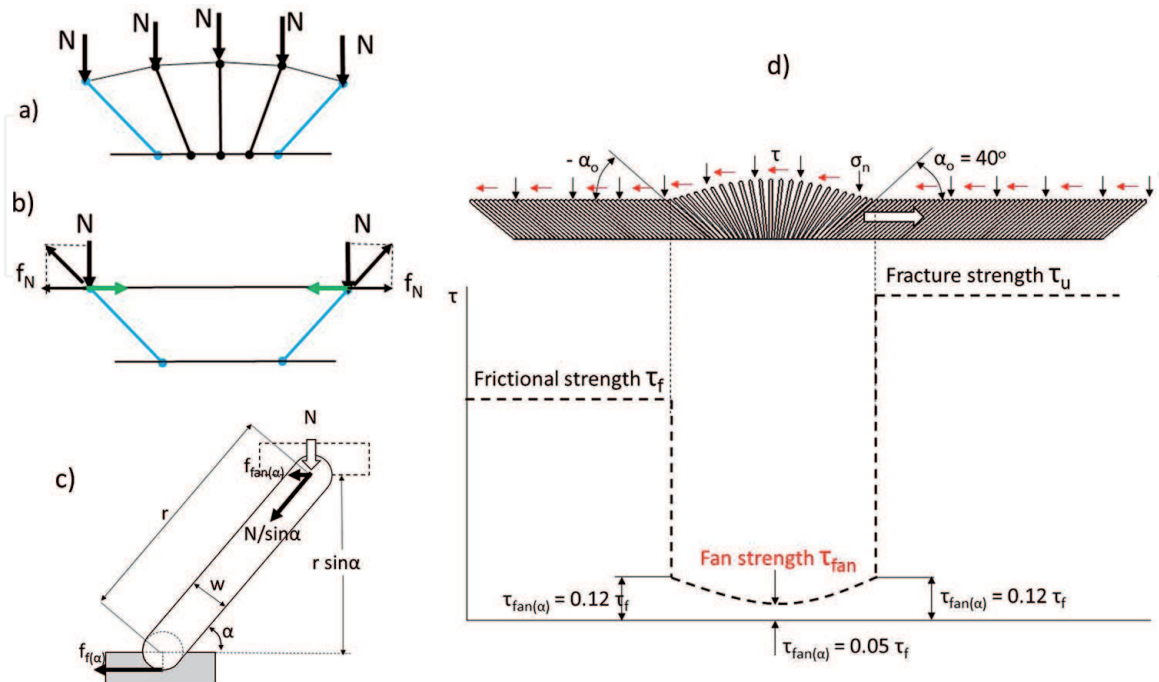


**Figure 7.** Schematic explanation of the reasons for the low shear resistance of the fan structure. a) and b) Principle of self-balancing of the fan structure. c) Friction in joints of domino blocks. d) Distribution of shear resistance along the fault involving the fan structure.



In order to cause the spontaneous rupture propagation through intact rock, the fan structure should provide, in addition to low shear resistance of the rupture head, also high shear stresses in the rupture tip and sufficiently high driving power at very low shear stresses applied. The next section explains unique principles involved by the fan mechanism to satisfy these requirements.

### 3.3 Low shear resistance, high stress amplification and driving power generated by the fan mechanism

First, we will analyse the reason for the low shear resistance of the fan structure. Domino blocks in the fan are interconnected by the rupture faces and behave as hinges between the moving (sliding) rupture faces. Shear resistance of the fan structure  $\tau_{\text{fan}}$  represents the resistance to displacement of the rupture faces relative to each other in the rupture head. **Figure 7** explains schematically the main principle responsible for low shear resistance of the fan structure. **Figure 7a** shows that all domino blocks in the fan are loaded by elementary forces  $N$  representing the normal stress  $\sigma_n$ . Elementary forces  $N$  applied to domino blocks in the front part of the fan resist to rotation of them. At the same time, elementary forces  $N$  applied to domino blocks in the rear part of the fan assist to rotation of these blocks. The key feature of the fan structure is the fact that each domino block in the front part of the fan is balanced by a symmetrical block of the rear part of the fan (**Figure 7b**). This means that the resistance to shear of this structure even at very high levels of normal stress applied will be determined solely by friction in joints.

**Figure 7c** allows estimating roughly friction in joints. It shows a self-balancing domino block (representing the right block in **Figure 7b**) of length  $r$  and width  $w$  with cylindrical ends rotating with sliding friction in corresponding cylindrical grooves. The block is inclined at an angle  $\alpha$  and loaded by force  $N$ . An analysis conducted in [20] shows that the presence of domino blocks between the shearing rupture faces decreases the resistance to shear compared with the conventional frictional sliding in accordance with Eq. (2):

$$\tau_{\text{fan}(\alpha)} = \tau_f w / r 2 \sin^2 \alpha \quad (2)$$

Eq. (2) shows that the resistance to shear  $\tau_{\text{fan}(\alpha)}$  between the rupture faces separated by self-balancing domino blocks and loaded by normal force  $N$  is determined by the conventional sliding friction  $\tau_f$ , the ratio  $w/r$  and the angle  $\alpha$  of the block inclination. Using Eq. (2) we can estimate the character of distribution of shear resistance between two rupture faces along the fan structure consisting of domino blocks characterised by the ratio  $w/r = 0.1$  and by the initial (and final) angle  $\alpha_0 = 40^\circ$  as shown in **Figure 7d**. According to Eq. (2), the largest shear resistance  $\tau_{\text{fan}(\alpha)} = 0.12 \tau_f$  is provided by the front and the rear domino blocks of the fan. The minimum shear resistance  $\tau_{\text{fan}(\alpha)} = 0.05 \tau_f$  is at the middle of the fan. The dotted curve in **Figure 7d** shows the distribution of shear resistance along the fan structure. In front of the fan, shear resistance is determined by the material strength  $\tau_s$ , and behind the fan it corresponds to the frictional strength  $\tau_f$ . Due to a small variation in shear resistance in the fan zone, we can describe the average strength of the fan structure by Eq. (3):

$$\tau_{\text{fan}} \approx \tau_f w / r \quad (3)$$

For the ratio  $w/r = 0.1$ , we will have

$$\tau_{\text{fan}} \approx 0.1 \tau_f \quad (4)$$



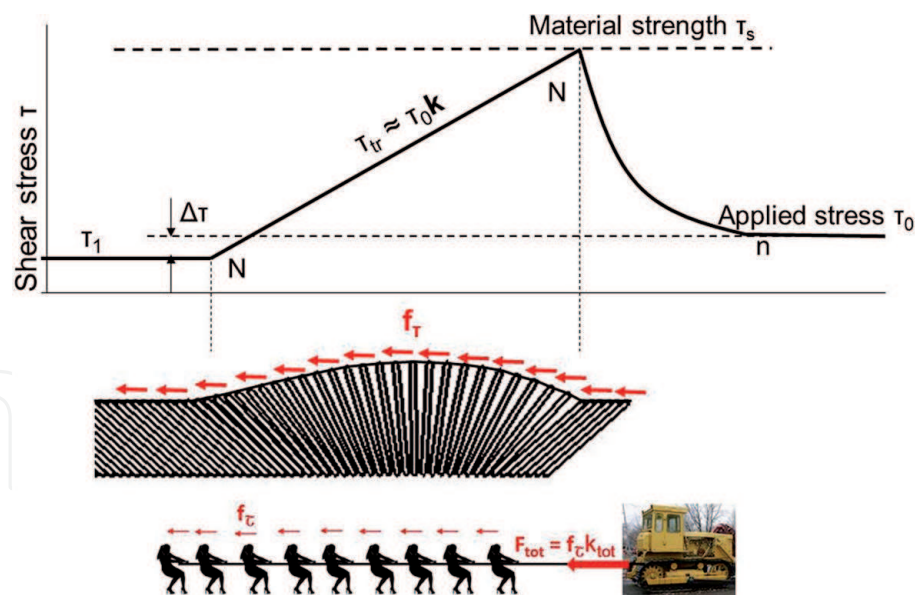


**Figure 8.**  
*Principles of shear stress amplification by the fan mechanism.*

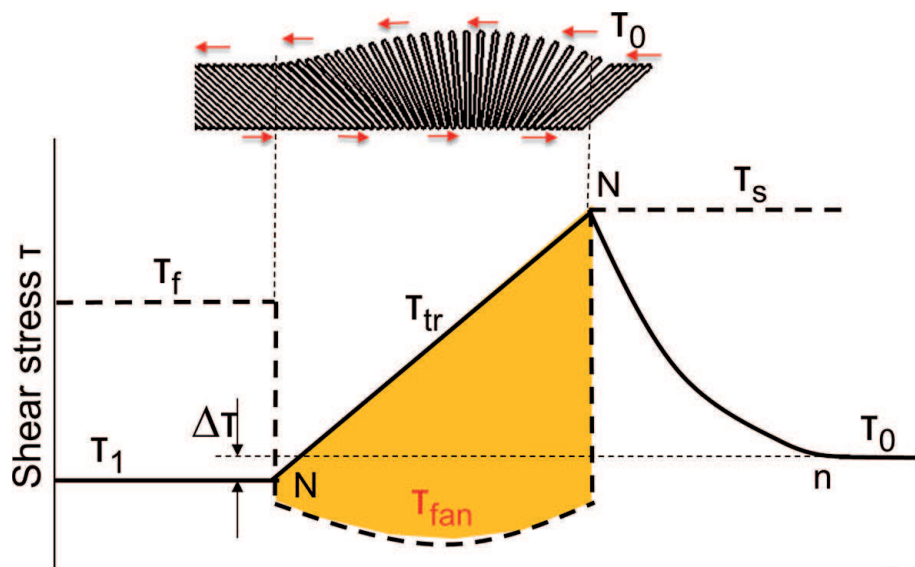


**Figure 9.**  
*Relative distribution of shear resistance and amplified shear stresses in the rupture head caused by the fan mechanism.*

This estimation is in accord with experimental results obtained on the physical model.

**Figure 8** illustrates schematically the unknown before and very powerful principle of shear stress amplification inherent in the fan mechanism. It shows the fan structure propagating from left to right through the intact material under the effect of distributed shear stress  $\tau_0$  applied to the whole fault. Behind the fan, domino blocks completed their rotation and form the frictional zone. The horizontal line  $\tau_0$  on the graph above the fan indicates the level of applied shear stress that is significantly less than the material strength  $\tau_s$ . The explanation on how the fan mechanism can provide high stresses equal to  $\tau_s$  in the rupture tip at very low shear stresses applied  $\tau_0$  is as follows.

All domino blocks of the fan structure are loaded by elementary forces  $f_\tau$  representing the applied shear stress. Within the fan zone, domino blocks are separated. Due to this, elementary forces  $f_\tau$  applied to each block cause corresponding rotation of them and stretch the elastic connector (i.e. the upper rupture face) in front

of each block, thus transmitting these forces to the rupture tip. This principle is similar to one shown below the fan. According to this principle, real forces affecting domino blocks within the fan zone increase towards the front as shown on the graph above the fan structure (line NN). This means that shear stress within the fan zone increases from the level  $\tau_1$  at the rear end of the fan towards the rupture tip approximately in proportion to the number of domino blocks  $k$  involved in the fan structure. We will call this stress as the fan-transient stress:  $\tau_{tr} \sim \tau_1 k$ . Analysis conducted in [18–20] shows that shear ruptures propagating in real materials can involve the fan structure with about a thousand of domino blocks. This means that the potential ability of the fan mechanism in stress amplification can be very large, but the real generated stresses are limited by the material strength.

**Figure 9** illustrates the relation between shear resistance and stresses generated by the fan mechanism at low shear stresses applied. A shaded curve here reflects the distribution of shear resistance along a fault involving the fan structure. In front of the fan, shear resistance corresponds to the material strength  $\tau_s$ , behind the fan it is determined by friction  $\tau_f$  and in the fan zone shear resistance is significantly less than the frictional strength  $\tau_{fan} \ll \tau_f$ . A solid curve reflects the shear stress variation. This schema shows that the fan mechanism can provide the rupture development at very low shear stresses applied  $\tau_0$  which can be significantly below the frictional strength, i.e. at  $\tau_{fan} < \tau_0 \ll \tau_f$ . The coloured area here represents symbolically the power generated by the fan mechanism that causes spontaneous rupture development even at low shear stresses applied. The instability is resulted from the fact that in the fan zone the generated stress exceeds the shear resistance and in the rupture tip it corresponds to the material strength.

It should be emphasised that despite the fact that the shear rupture here propagates through ‘intact’ material, the magnitude of stress drop  $\Delta\tau = \tau_0 - \tau_1$  can be very low (lower than at the frictional stick-slip instability) because the rupture propagates at low shear stresses applied  $\tau_0 \ll \tau_f$ . Depending on the level of  $\tau_0$ , the fan mechanism can provide two types of rupture mode (crack-like and pulse-like) observed in natural and laboratory earthquakes [4, 31, 32]. This question

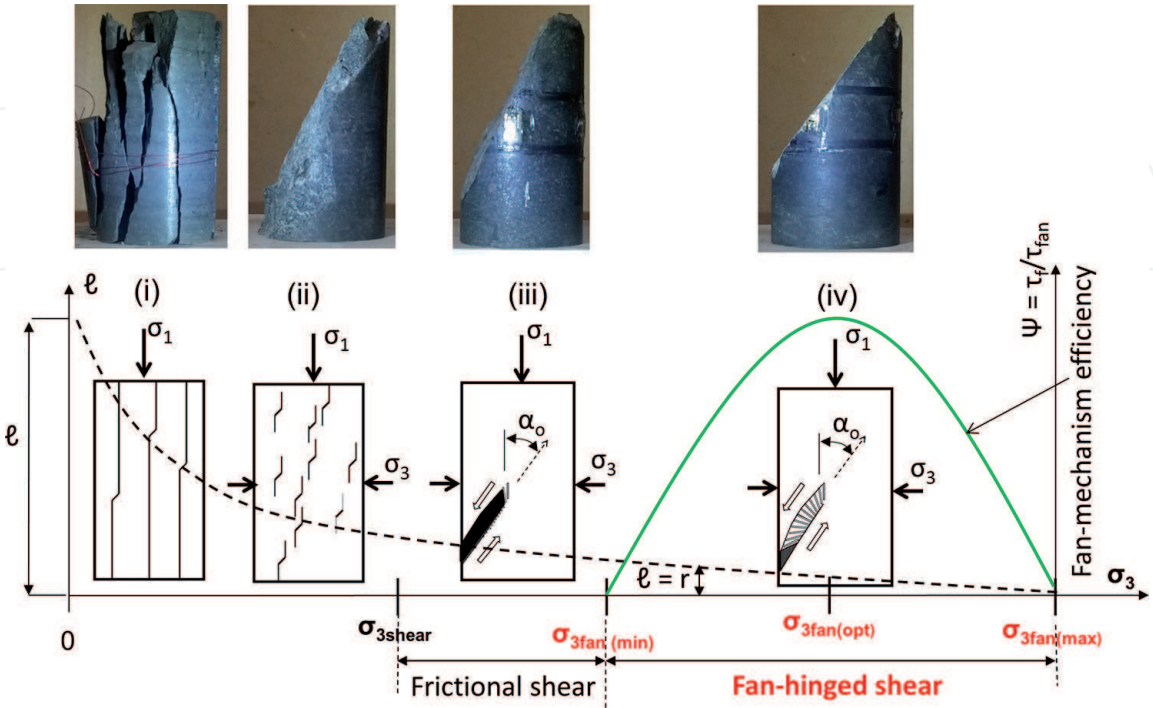


**Figure 10.** The evolution of failure mechanisms in hard rocks with rising confining pressure  $\sigma_3$  and variable efficiency of the fan mechanism within the pressure range  $\sigma_{3fan(min)} < \sigma_3 < \sigma_{3fan(max)}$ .

is discussed in [19, 20]. The fan mechanism explains also the heat flow paradox observed for extreme ruptures [6, 13].

### 3.4 Reasons for the fan-mechanism operation at high $\sigma_3$ and new strength profiles for hard rocks

**Figure 10** illustrates the evolution of failure mechanisms in hard rock specimens with rising  $\sigma_3$ . Confining pressure  $\sigma_3$  increases along the horizontal axis from left to right. At the origin of the horizontal axis,  $\sigma_3 = 0$ . The basic point is that the failure process of brittle rocks at any level of  $\sigma_3$  is accompanied by formation of tensile cracks; however, the ultimate length  $\ell$  of tensile cracks that can be developed at failure depends on the level of  $\sigma_3$  because rising  $\sigma_3$  suppresses the tensile crack growth. A dotted curve here shows symbolically the typical variation of ultimate length  $\ell$  of tensile cracks as a function of  $\sigma_3$ : the higher the  $\sigma_3$ , the shorter the  $\ell$ . The length  $\ell$  of tensile cracks in turn determines the macroscopic failure mechanism and the failure pattern shown schematically in rock specimens (i)–(iv).

Within the pressure range  $0 \leq \sigma_3 < \sigma_{3\text{shear}}$  shear rupture cannot propagate in its own plane due to creation at the rupture tip of relatively long tensile cracks that prevent the shear rupture propagation. The following two basic principles of the failure process taking place within this pressure range may be distinguished:

- i. Splitting by long tensile cracks (at low  $\sigma_3$ )
- ii. Distributed microcracking followed by coalescence of microcracks (at larger  $\sigma_3$ )

At  $\sigma_3 \geq \sigma_{3\text{shear}}$  the failure mode is localised shear. Here high enough confining pressure  $\sigma_3$  suppresses the formation of long tensile cracks, and tensile cracks generated in the rupture tip become sufficiently short to assist shear rupture to propagate in its own plane. The fracture front moves through the rock due to creation of an echelon of micro-tensile cracks in the fracture tip and inter-crack slabs (domino blocks) which are subjected to rotation at shear displacement of the rupture faces. Here, depending on behaviour of domino blocks at rotation, two basic principles of the failure process may be distinguished as discussed in **Figure 4**:

- iii. Frictional shear—characterised by collapse of insufficiently short domino blocks (at  $\sigma_{3\text{shear}} \leq \sigma_3 \leq \sigma_{3\text{fan}(\text{min})}$ )
- iv. Fan-hinged shear—associated with formation of the fan structure consisting of sufficiently short domino blocks (of length  $r = \ell$  and width  $w$ ) and withstanding rotation without collapse (at  $\sigma_3 > \sigma_{3\text{fan}(\text{min})}$ )

An important fact is that the fan mechanism exhibits different efficiency depending on the level of  $\sigma_3$ . We will determine the fan-mechanism efficiency as the ratio between the frictional strength and the fan strength:  $\psi = \tau_f / \tau_{\text{fan}}$ . The point is that the length  $r$  of domino blocks decreases with rising  $\sigma_3$ . At confining pressure near  $\sigma_{3\text{fan}(\text{min})}$ , when the relative length ( $r/w$ ) of domino blocks is still relatively large, the blocks are subject to partial destruction as they rotate. In this case the fan-mechanism efficiency is quite low. At higher  $\sigma_3$ , with shorter blocks, this imperfection decreases, rendering the fan mechanism more efficient. The optimal efficiency takes place at  $\sigma_{3\text{fan}(\text{opt})}$  when the blocks with an optimal ratio  $r/w$  rotate with minimum destruction. At greater  $\sigma_3$  the efficiency reduces because shorter blocks gradually lose their potential for operation as hinges. Finally very short blocks lose this capability completely, and the rock behaviour returns to the conventional frictional mode. This happens at  $\sigma_{3\text{fan}(\text{max})}$ . The green curve in **Figure 10** illustrates



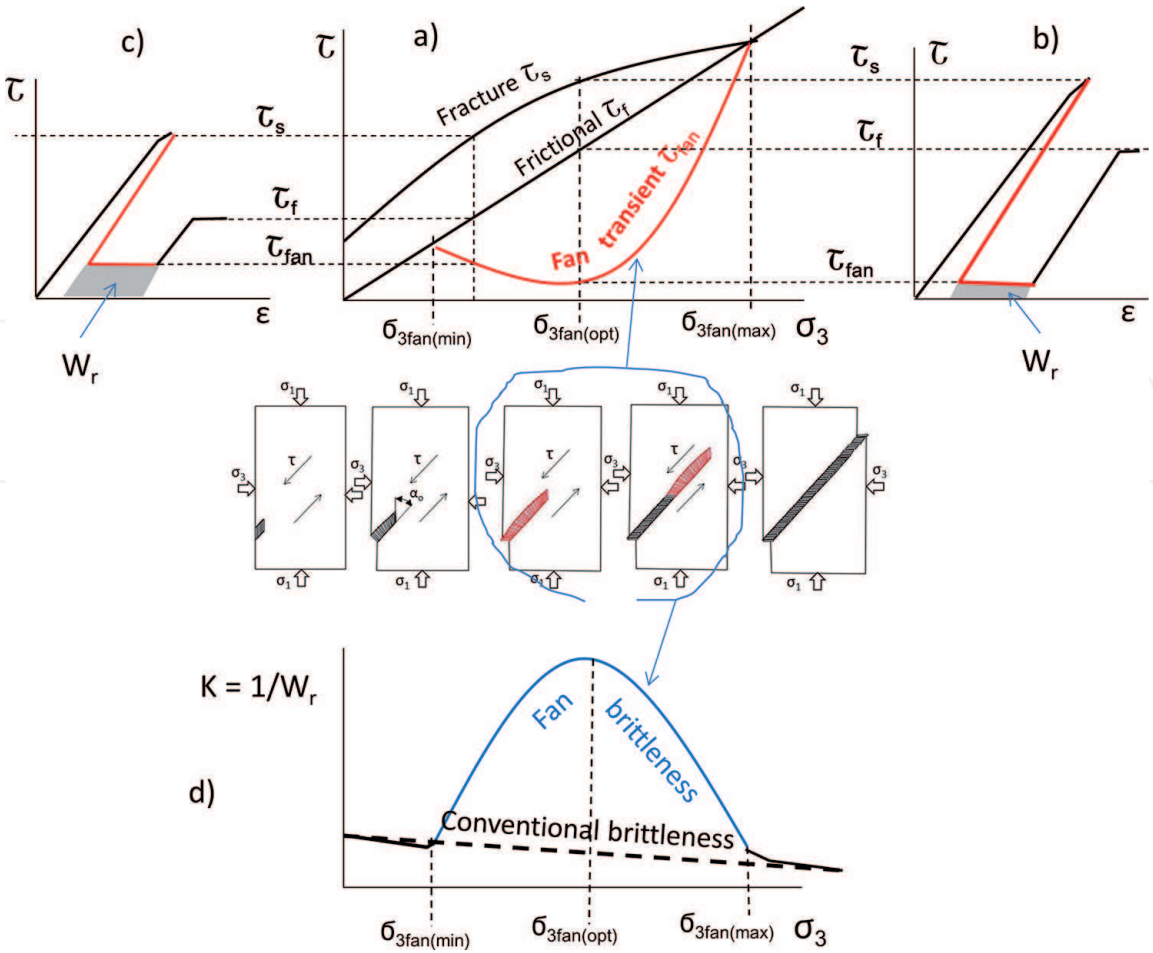


**Figure 11.** Strength profiles and brittleness profiles for hard rocks. a), b) and c) Strength profiles for  $\tau_s$ ,  $\tau_f$  and  $\tau_{fan}$  plotted on the basis of complete stress-strain curves. d) Difference between the conventional and new understanding of rock brittleness variation with rising  $\sigma_3$ .

graphically a possible variation of the fan-mechanism efficiency  $\psi = \tau_f/\tau_{fan}$  versus confining stress  $\sigma_3$ .

The variable efficiency of the fan mechanism with  $\sigma_3$  causes corresponding variation in the transient strength and brittleness of hard rocks. **Figure 11a** shows schematically an improved model of strength profiles involving conventional fracture  $\tau_s$  and frictional  $\tau_f$  strength profiles and the transient fan strength  $\tau_{fan}$  profile (red curve). Stress-displacement curves in **Figure 11b** and **c** reflecting real post-peak rock properties (shown in red) explain the meaning of the fan strength profile and its variation versus  $\sigma_3$ . **Figure 11b** corresponds to the situation at  $\sigma_3 = \sigma_{3fan(opt)}$  where the fan mechanism exhibits the maximum efficiency. At peak stress the material strength is  $\tau_s$ . After completion of the fan structure, the specimen strength decreases to the level  $\tau_{fan}$  representing the transient material strength. This means that the shear fracture governed by the fan mechanism can propagate through the material at any level of shear stress above  $\tau_{fan}$ . After the fan has crossed the specimen body, the specimen strength is determined by the frictional strength  $\tau_f$  of the new fault. For confining pressures  $\sigma_3 < \sigma_{3fan(opt)}$  or  $\sigma_3 > \sigma_{3fan(opt)}$  the fan-mechanism efficiency is lower. The graph in **Figure 11c** indicates the relative values of  $\tau_s$ ,  $\tau_f$  and  $\tau_{fan}$  and their positions on the profiles for the situation where  $\sigma_3 < \sigma_{3fan(opt)}$ .

Let us analyse how the variable efficiency of the fan mechanism can affect the rock brittleness. In the simplest case, the brittleness of the same rock for different testing conditions can be estimated as the reciprocal of the specific rupture energy associated with the rupture propagation governed by the fan mechanism through



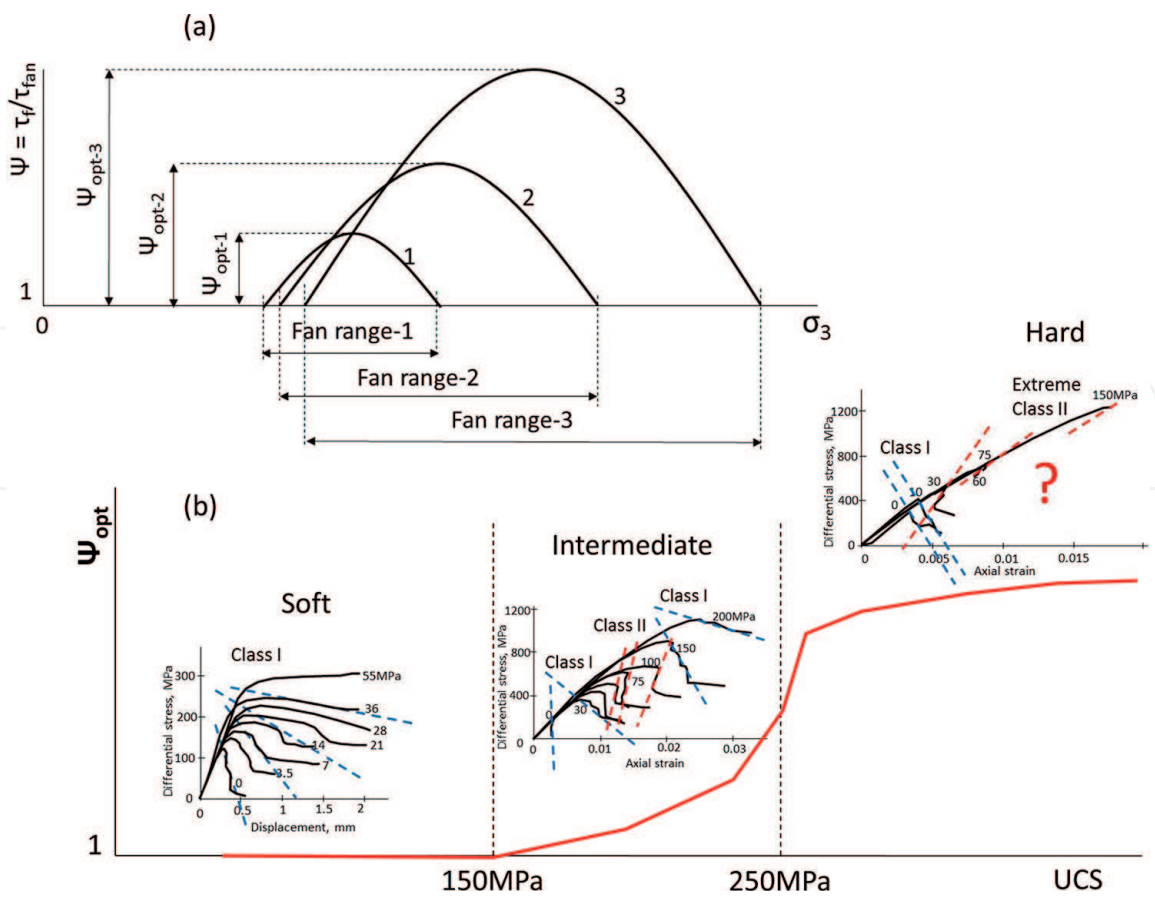


**Figure 12.**  
(a) Variation of the fan-mechanism efficiency  $\psi = \tau_f / \tau_{fan}$  versus confining pressure  $\sigma_3$  for rocks of different hardness (UCS). (b) Variation of the optimal efficiency of the fan mechanism  $\psi_{opt}$  versus UCS.

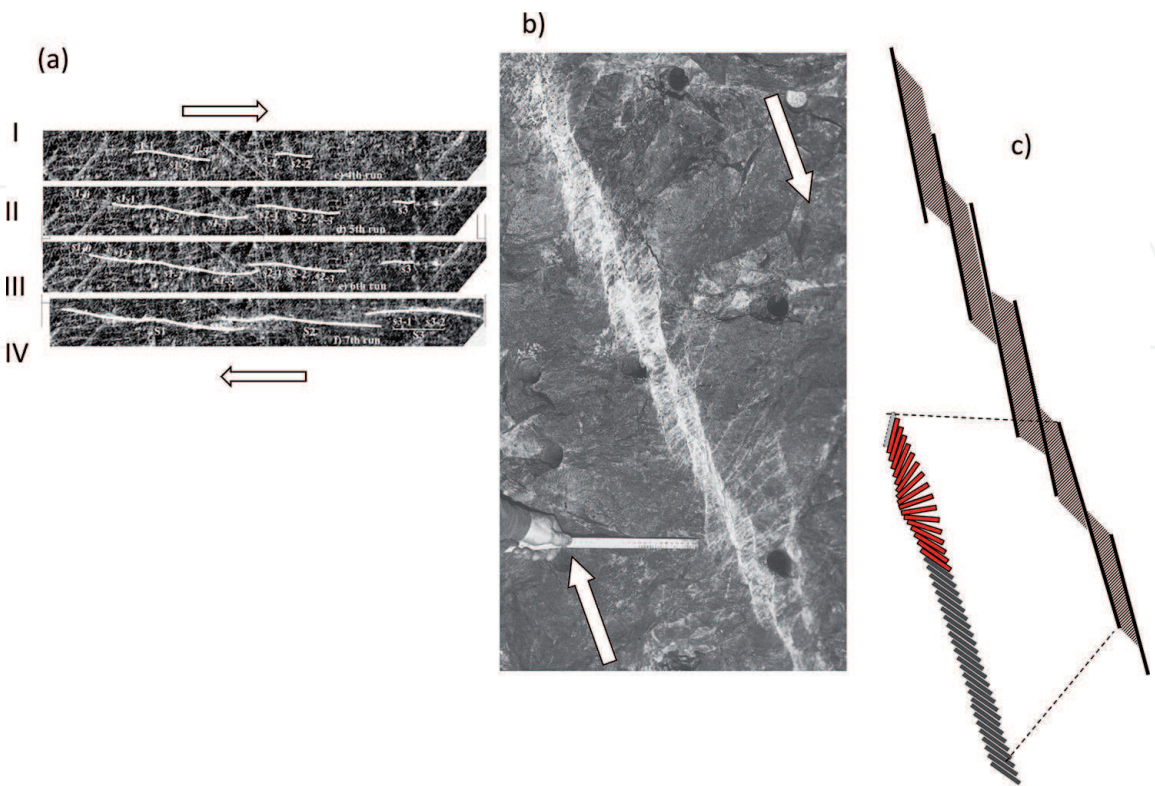


**Figure 13.**  
a) Shear rupture propagation by advanced triggering of new segments (modified photograph from [29]). b) and c) Principle of formation of the domino and fan structure in segmented faults.

intact rock. Shaded areas on stress-strain curves in **Figure 11b** and **c** represent the specific rupture energy  $W_r$  for different  $\sigma_3$ . The brittleness index  $K = 1/W_r$  can be used to characterise the brittleness variation versus  $\sigma_3$ . The shaded line in **Figure 11d** illustrates symbolically the conventional understanding of rock brittleness variation in accordance with which the rising confining pressures  $\sigma_3$  make rock less brittle. Because the fan mechanism decreases dramatically the specific rupture energy within the pressure range  $\sigma_{3fan(min)} < \sigma_3 < \sigma_{3fan(max)}$ , the brittleness at these stress conditions should be significantly higher than the conventional understanding. The blue curve in **Figure 11d** indicates the character of rock embrittlement caused by the fan mechanism. Estimations made in [17, 22] show that at high  $\sigma_3$  rock brittleness can be a hundred of times higher than at low  $\sigma_3$ . At  $\sigma_3 = \sigma_{3fan(opt)}$  rock conditions can be super brittle.

The fan-mechanism efficiency  $\psi = \tau_f/\tau_{fan}$  depends also on the rock hardness characterised by UCS. **Figure 12a** shows three curves indicating variations of  $\psi = \tau_f/\tau_{fan}$  versus  $\sigma_3$  for three rocks of different hardness. Here the harder the rock, the greater the optimal fan-mechanism efficiency  $\psi_{opt}$  and the larger the range of  $\sigma_3$  where the fan mechanism is active. The red curve in **Figure 12b** illustrates symbolically the dependence of the optimal efficiency of the fan mechanism  $\psi_{opt}$  on the hardness (UCS) of different rocks. The fan mechanism operates with the largest efficiency in rocks with UCS > 250 MPa. Within the range of UCS 150–250 (roughly), the efficiency is significantly lower. In soft rocks the fan mechanism is not active.

## 4. Fan mechanism as a source of dynamic events in the earth's crust

### 4.1 Features of the fan-structure formation in complex natural faults

This section discusses the role of the fan mechanism in generation of shallow earthquakes and shear rupture rockbursts in deep mines. In the previous sections, we introduced different unique features of the fan mechanism and 'abnormal' properties of hard rocks. All analysis was conducted for primary shear ruptures which are thin and continuous. Unlike primary ruptures natural faults typically have very complicated segmented and multi-hierarchical structure [7, 33, 34]. Main principles of the complex fault evolution in association with the fan mechanism were discussed in [20, 23, 35]. Here we will outline briefly most important features of the fan-mechanism generation in complex faults.

It was observed that in ultra-deep South African mines, very severe dynamic events (shear rupture rockbursts) are caused by new shear ruptures generated in pristine rock [36, 37]. These mine tremors are seismically indistinguishable from natural earthquakes and share the apparent paradox of failure under low shear stress [37]. Photographs of such faults are shown in **Figure 5b**. The structure of all these faults is identical consisting of a row of domino blocks. However, the domino structure is more complex than in primary ruptures.

**Figure 13** explains features of this structure formation. Series of photographs in **Figure 13a** (modified from [38]) shows principles of segmented fault propagation observed experimentally. The fault propagates due to advanced triggering of new segments. The photographs show four stages (I–IV) of the fault evolution. Segments are represented here by white lines. The fault propagates from left to right. The segments are generated one by one due to the stress transfer and propagate bilaterally. At the meeting of each two neighbouring segments, they are connected by a compressive jog. It was found out in [29, 38] that jogs of the compression type are very common at high confining pressures to fault zones regardless of their sizes. Overlap zones of the jogs

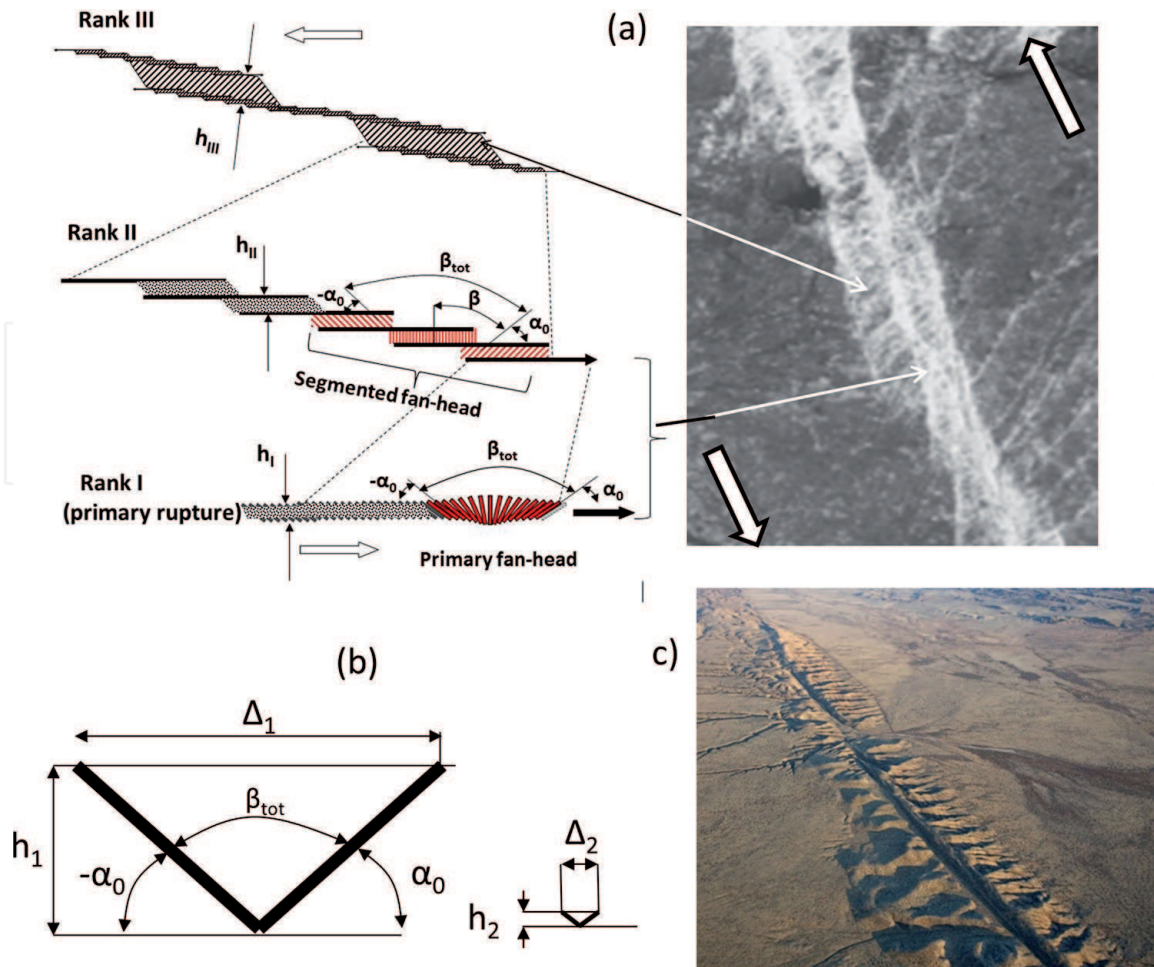


**Figure 14.**

*The fan mechanism is predominantly activated in fault segments of lower hierarchical ranks (schematic illustration) providing extreme dynamics along thin localised zones.*

are subjected to significant irreversible deformation. **Figure 13b** and **c** demonstrates that in brittle rocks the irreversible deformation in jogs is associated with formation of a row of domino blocks (modified photograph from [29]). The general fault here consists of a number of segments represented by primary ruptures. The propagation of primary ruptures in hard rocks at high  $\sigma_3$  is governed by the fan mechanism.

The domino structure of the next hierarchical ranks can also be involved in the fan-structure formation. This feature is illustrated in **Figure 14**. It was observed in [38] that segmentation as a mechanism of fault propagation acts on all hierarchical ranks of complex faults. Once a number of segments of a given hierarchical rank coalesce, they behave as a whole as a new and longer segment of one higher rank. Segment of higher rank can trigger a new segment (shear fracture) at greater distance. A photograph in **Figure 14a** (modified from [29]) shows a fault fragment involving segments of three hierarchical ranks. The structure of this fault is shown symbolically on the left. It incorporates primary ruptures and higher rank segments formed on the basis of compressive jogs represented by the domino structure (rank II and rank III). Domino blocks involved in segments of higher rank can form the fan structure similar to primary ruptures due to rotation of them caused by shear displacement of the rupture faces. However, the complete fan structure can be formed if shear displacement between the fault faces  $d_{\text{fault}}$  is sufficient for the completed block rotation.

**Figure 14b** shows the initial and final positions of domino blocks for two shear ruptures of thicknesses  $h_1$  and  $h_2$ . The thick rupture requires significantly



greater displacement  $d_{\text{fault}} = \Delta$  to complete the block rotation. Due to this, the complete fan structure (red zones in **Figure 14a**) is predominantly created in segments of lower ranks. The fan mechanism generated here creates high dynamics of the failure process. Relatively thin localised zones of very intense destruction can be observed in each dynamic fault. The initial domino structure of these segments is completely destroyed by extensive and violent shear and represented by pulverised gouge. In high-rank segments, domino blocks rotate by low angles without formation of the fan structure and assist the accommodation of displacement along the whole fault. The domino-like structure is typical for faults of very different scales including laboratory specimens, shear rupture rockbursts in mines and earthquakes. Two photographs in **Figure 14a** and **c** show identical domino structure of two dynamic faults which generated severe shear rupture rockburst (a South African ultra-deep mine) and earthquake (the San Andreas fault exposed on land) [39].

**4.2 Generation of new faults in intact rock at low shear stresses nearby a pre-existing fault caused by the fan mechanism**

This section proposes an alternative explanation to the fact that earthquakes are commonly attributed to pre-existing faults. Pre-existing discontinuities play the role of local stress concentrators, creating the starting conditions for the fan-structure formation. After completion of the initial fan structure, it can create a new dynamic fault in the form of earthquake by propagation through intact rock mass loaded by low shear stresses. **Figure 15** illustrates one of the many models for generation of high local stress on the basis of pre-existing fault. It shows a rock fragment involving a pre-existing fault (black line) with a compressive jog. This

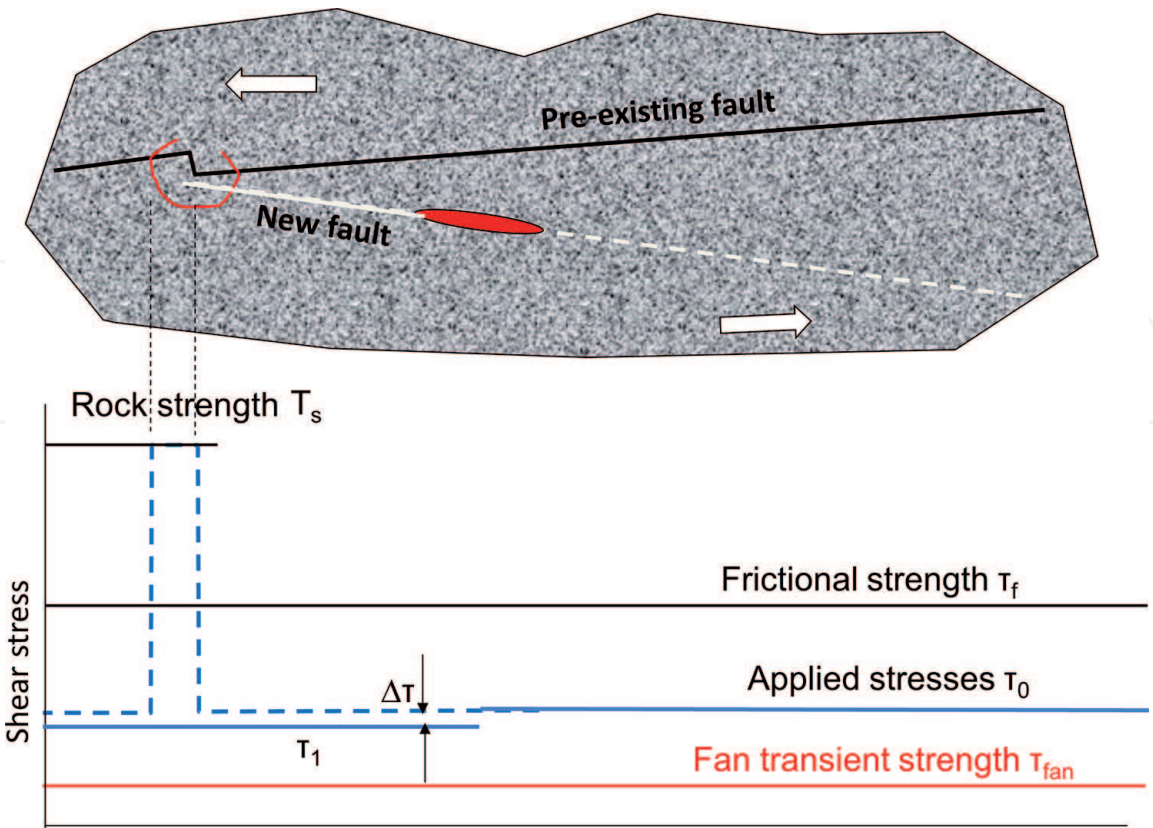


**Figure 15.**  
*Features of generation of a new extreme rupture in pristine hard rock in the vicinity of a pre-existing fault at low field shear stresses caused by the fan mechanism.*



fragment is located at great depth where the minor stress  $\sigma_3$  is high enough for the fan-mechanism activation in intact rock. Horizontal lines on the graph below indicate symbolically levels of the following parameters:  $\tau_s$  is the strength of intact rock,  $\tau_f$  is the frictional strength of pre-existing fault,  $\tau_{fan}$  is the transient strength of intact rock determined by the fan mechanism,  $\tau_0$  is the field shear stress applied to the rock fragment,  $\tau_1$  is the field stress after the rupture propagation and  $\Delta\tau$  is the stress drop. Orientation of the field shear stress is shown by open arrows.

Because the level of field stress  $\tau_0$  is significantly less than the frictional strength  $\tau_f$ , the situation on the pre-existing fault is very stable. However, due to deformations along the fault caused by shear stresses  $\tau_0$ , a high local stress can be created in the jog zone delineated by a red circle. If the local stress in intact rock of this zone reaches the level of rupture strength  $\tau_s$ , the fan structure can be formed. After formation of the fan structure, it can propagate spontaneously through intact rock mass at low shear stresses  $\tau_0$  in accordance with Class III behaviour discussed in **Figure 3** and generate an earthquake. The new fault is shown by a white line, and the propagating fan head is represented by red ellipsis. Due to very high brittleness of this rock associated with extremely low rupture energy provided by the fan mechanism, the failure process can be accompanied by abnormal energy release and violence. It should be emphasised that despite the fact that the new fault is formed in intact rock, the magnitude of stress drop  $\Delta\tau$  can be very low because this process takes place at low shear stress applied. The stress drop can be even less than at the stick-slip process in the case of activation of the pre-existing fault.

Thus, the fan mechanism favours the generation of new faults in hard intact rock mass adjoining a pre-existing fault in preference to frictional stick-slip instability along the pre-existing fault. Each earthquake generated by the fan mechanism is associated with formation of a new fault at a new location in the vicinity of a pre-existing fault. Furthermore, each new fault can serve as a stress concentrator for generation of the next new fault. The proximity of the pre-existing fault to the zone of dynamic new fracture development in intact rock creates the illusion of frictional stick-slip instability of the pre-existing fault, thus concealing the real situation.

At the same time, there are many evidences that earthquakes are associated with the formation of new faults in the proximity of pre-existing faults. For example, **Figure 16** shows maps of earthquakes in a New Zealand region of relative motions between the Australian and Pacific plates which are not accommodated on one general fault, but on many faults across a wide zone. **Figure 16a** (from [40]) shows

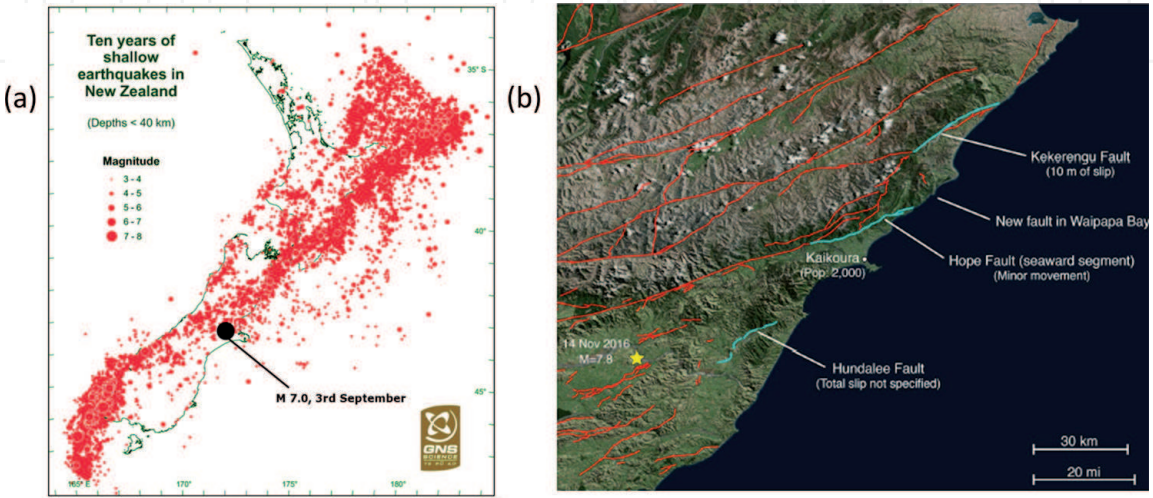


**Figure 16.**  
*Maps of spatial distribution of earthquake hypocentres and faults on the earth's surface for a New Zealand region [40, 41].*

spatial distribution of hypocentres at depths <40 km. Some earthquake faults generated at great depths can reach the earth's surface as shown in **Figure 16b** (from [41]). The formation of each fault from reaching the earth's surface is associated with an earthquake. The fan mechanism which makes intact hard rocks weaker in respect of dynamic shear rupturing than pre-existing faults is responsible for the spatial distribution of earthquake hypocentres and for the fact that the earth's crust is riddled with faults. A series of aftershocks, which usually accompany the main act of an earthquake, can also be explained by the formation of a series of new faults, where each new fault creates the conditions for activating the fan mechanism in the adjacent zone of intact rock.

**4.3 Depth distribution of rock strength, brittleness and earthquake activity caused by the fan mechanism**

**Figure 17d** shows a typical histogram of depth distribution of earthquake frequency (from [7]). It demonstrates that earthquake activity varies with depth and has a maximum at a certain depth. Today there are two fundamentally different explanations for this earthquake feature. Both of them consider earthquakes as stick-slip instability on pre-existing faults. The first one is based on the fact that the frictional strength (determining the lithospheric strength) in the upper crust increases with depth in accordance with Byerlee's friction law [10], while in the lower crust it decreases accordingly to a high-temperature steady-state flow law [2, 7]. The second one is based on the velocity-weakening and velocity-strengthening concept [7, 9]. We introduce here a new concept which is based on the new understanding about (unknown before) properties of hard rocks at seismic depth's caused by the fan mechanism [20, 23, 42].

**Figure 17a–c** shows symbolically depth distribution of the fan-mechanism efficiency, rock strength profiles and rock brittleness. These graphs are analogous to the dependencies discussed in **Figures 11** and **12**. The fan mechanism can operate at depths where temperature (rising with depths) does not prevent the fan-hinged shear. The new strength profile for hard rocks in **Figure 17b** shows that at low depths corresponding to  $\sigma_3 < \sigma_{3fan(min)}$ , the lithospheric strength is determined solely by frictional strength  $\tau_f$ . At greater depths corresponding to the range of the fan-mechanism activity, the situation is specific. In the absence of conditions for

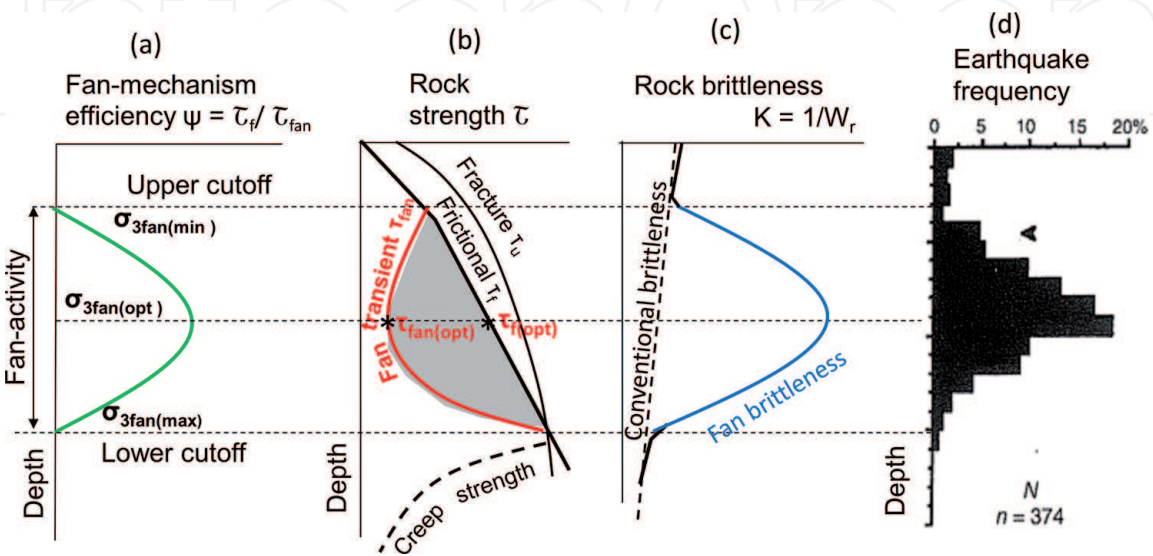


**Figure 17.**  
*Relation between depth distribution of the fan-mechanism efficiency, rock strength, rock brittleness and earthquake frequency.*

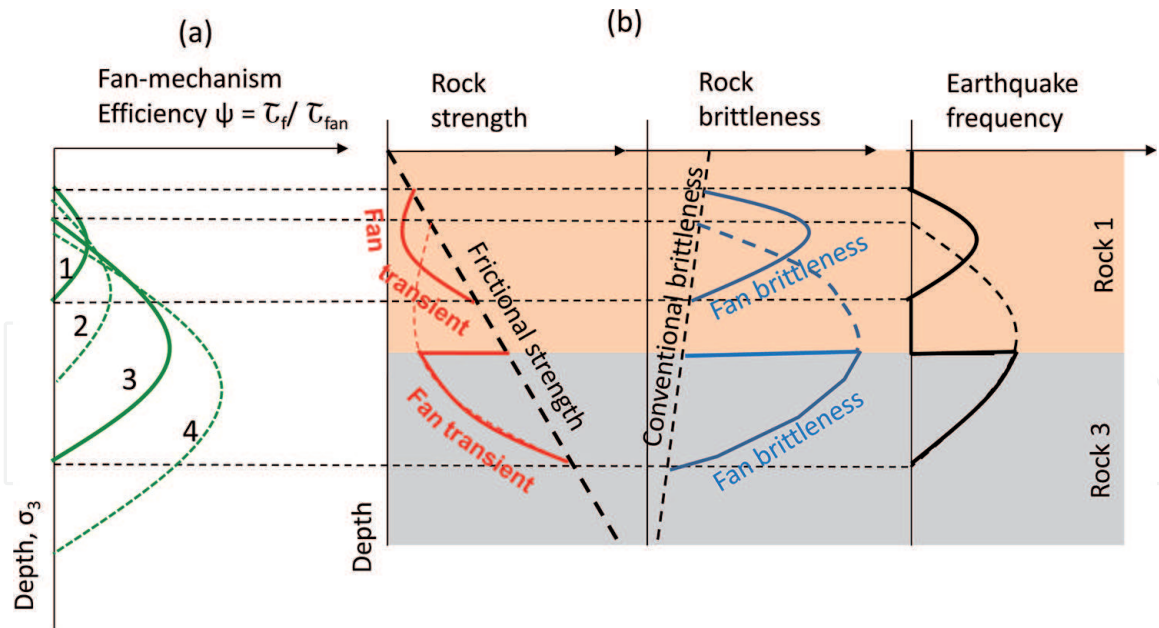


**Figure 18.**

*Illustration of depth distribution for rock transient strength, brittleness and earthquake frequency in the Earth's crust represented by two layers of rocks of different hardness.*

activation of the fan mechanism, the lithospheric strength is determined by friction. However, if the fan mechanism is activated somewhere causing the new rupture development in intact rock, the transient lithospheric strength in that region decreases to the level  $\tau_{fan}$ . After completion of the failure process, the lithospheric strength returns to the frictional strength.

It should be noted that the improved concept of the lithospheric strength incorporates all three types of rock strength determining the instability in the seismic layer: fracture strength  $\tau_s$ , frictional strength  $\tau_f$  and fan strength  $\tau_{fan}$ . The fracture strength determines the level of local stress at which the initial fan structure can be generated. The shaded area between the frictional  $\tau_f$  and the fan-transient  $\tau_{fan}$  profiles determines levels of field stress under which an initiated fan structure can propagate creating an earthquake. Importantly, the fan mechanism can cause earthquakes at any level of field stress  $\tau$  within the shaded zone. Due to this the highest probability of events is at a depth characterised by the maximum range between  $\tau_{fan}$  and  $\tau_f$ . This depth corresponds approximately to the depth of optimal efficiency of the fan mechanism, where the rock mass is characterised by the minimum transient strength and maximum brittleness. At lower and greater depths, the probability decreases. This feature determines the typical depth-frequency distribution of earthquake hypocentres. The upper and lower cut-offs represent boundaries of the zone of the fan-mechanism activity. The explanation for the depth distribution of earthquake frequency on the basis of the fan mechanism differs fundamentally from the conventional explanations.

On the basis of the fan mechanism, it is possible also to explain the existence of a few zones of earthquake activity with depth. As discussed in **Figure 12**, the efficiency of the fan mechanism depends on the rock hardness (UCS): the harder the rock, the greater the fan-mechanism efficiency and the wider the confining pressure range over which the fan mechanism is active. **Figure 18a** illustrates schematically depth distributions of the fan-mechanism activity for four rocks characterised by different hardness, with strength increasing from rock 1 to rock 4. **Figure 18b** shows a situation when the earth's crust is represented by two layers of rocks of different hardness (rock 1 and rock 3). In this case, two zones of earthquake activity may be observed. Rock 1 will exhibit the typical (complete) form of earthquake



frequency-depth distribution, while rock 3 will show a truncated form. Such features of earthquake behaviour have been observed in nature and explained on the basis of conventional velocity-weakening and velocity-strengthening approach [9].

The fan theory proposes new explanations for a number of other abnormalities and paradoxes associated with extreme rupture dynamics (including supershears) observed in natural and laboratory conditions [19, 20, 43]. Mathematical models were developed which allow studying unique features of the fan mechanism and simulating the process of extreme rupture development at different loading conditions [43–46].

## Acknowledgements

This work was supported by the Ministry of Science and Education of the Russian Federation (grant no. RFMEFI58418X0034).

## Author details

Boris Tarasov

The Far Eastern Federal University, Vladivostok, Russia

\*Address all correspondence to: [bgтарас@gmail.com](mailto:bgтарас@gmail.com)

## IntechOpen

© 2019 The Author(s). Licensee IntechOpen. This chapter is distributed under the terms of the Creative Commons Attribution License (<http://creativecommons.org/licenses/by/3.0>), which permits unrestricted use, distribution, and reproduction in any medium, provided the original work is properly cited. 



## References

- [1] Brace WF, Byerlee JD. Stick-slip as a mechanism for earthquakes. *Science*. 1966;**153**(3739):990-992
- [2] Brace WF, Kohlstedt D. Limits on lithospheric stress imposed by laboratory experiments. *Journal of Geophysical Research*. 1980;**85**:6248-6252
- [3] Ruina AL. Slip instability and state variable friction laws. *Journal of Geophysical Research*. 1983;**88**:10359-10370
- [4] Heaton TH. Evidence for and implications of self-healing pulses of slip in earthquake rupture. *Physics of the Earth and Planetary Interiors*. 1990;**64**(1):1-20
- [5] Dieterich JH. Earthquake nucleation on faults with rate-dependent and state-dependent strength. *Tectonophysics*. 1992;**211**:115-134
- [6] Ben-Zion Y. Dynamic ruptures in recent models of earthquake faults. *Journal of the Mechanics and Physics of Solids*. 2001;**49**:2209-2244
- [7] Scholz CH. *The Mechanics of Earthquakes and Faulting*. Cambridge: Cambridge University Press; 2002
- [8] Allmann BP, Shearer PM. Global variations of stress drop for moderate to large earthquakes. *Journal of Geophysical Research*. 2009;**114**:B01310. DOI: 10.1029/2008JB005821
- [9] Albaric J, Deverchere J, Petit C, Perrot J, Le Gall B. Crustal rheology and depth distribution of earthquakes: Insights from the central and southern East African Rift System. *Tectonophysics*. 2009;**468**:28-41
- [10] Byerlee JD. Friction of rocks. *Pure and Applied Geophysics*. 1978;**116**:615-626
- [11] Lachenbruch AH. Frictional heating, fluid pressure, and the resistance to fault motion. *Journal of Geophysical Research*. 1980;**85**:6097-6112
- [12] Dieterich JH, Conrad G. Effect of humidity on time- and velocity-dependent friction in rocks. *Journal of Geophysical Research*. 1984;**89**:4196-4202. DOI: 10.1029/JB089iB06p04196
- [13] Brown R. Frictional heating on faults: Stable sliding versus stick slip. *Journal of Geophysical Research*. 1998;**103**(B4):7413-7420
- [14] Di Toro G, Goldsby DL, Tullis TE. Friction falls towards zero in quartz rock as slip velocity approaches seismic rates. *Nature*. 2004;**427**:436-439
- [15] Ben-David O, Rubinstein SM, Fineberg J. Slip-stick and the evolution of frictional strength. *Nature*. 2010;**463**:76-79
- [16] Tarasov BG. Intersonic shear rupture mechanism. *International Journal of Rock Mechanics and Mining Science*. 2008;**45**(6):914-928
- [17] Tarasov BG. Super brittleness of rocks at high confining pressure. In: Van Sint Jan M, Potvin Y, editors. *Keynote addresses on Proceedings of the Fifth International Seminar on Deep and High Stress Mining*. Perth: Australian Centre for Geomechanics; 2010. pp. 119-133
- [18] Tarasov BG. Hitherto unknown shear rupture mechanism as a source of instability in intact hard rocks at highly confined compression. *Tectonophysics*. 2014;**621**:69-84
- [19] Tarasov BG. Shear fractures of extreme dynamics. *Rock Mechanics and Rock Engineering*. 2016;**49**(10):3999-4021
- [20] Tarasov BG. Shear ruptures of extreme dynamics in laboratory and

- natural conditions. In: Wesseloo J, editor. Keynote addresses on Eighth International Conference on Deep and High Stress Mining. Perth, ISBN: 978-0-9924810-6-3; 2017. pp. 1-48
- [21] Tarasov BG, Randolph MF. Frictionless shear at great depth and other paradoxes of hard rocks. *International Journal of Rock Mechanics and Mining Science*. 2008;**45**(3):316-328
- [22] Tarasov BG, Randolph MF. Super brittleness of rocks and earthquake activity. *International Journal of Rock Mechanics and Mining Science*. 2011;**48**:888-898
- [23] Tarasov BG, Randolph MF. Improved concept of lithospheric strength and earthquake activity at shallow depths based upon the fan-head dynamic shear rupture mechanism. *Tectonophysics*. 2016;**667**:124-143
- [24] Rummel F, Fairhurst C. Determination of the post-failure behavior of brittle rock using a servo-controlled testing machine. *Rock Mechanics and Rock Engineering*. 1970;**2**(4):189-204
- [25] Reches Z, Lockner DA. Nucleation and growth of faults in brittle rocks. *Journal of Geophysical Research*. 1994;**99**:18159-18173
- [26] Peng S, Johnson AM. Crack growth and faulting in cylindrical specimens of Chelmsford granite. *International Journal of Rock Mechanics and Mining Sciences*. 1972;**9**:37-86
- [27] Horii H, Nemat-Nasser S. Compression-induced micro-crack growth in brittle solids: Axial splitting and shear failure. *Journal of Geophysical Research*. 1985;**90**:3105-3125
- [28] King GCP, Sammis CG. The mechanisms of finite brittle strain. *Pure and Applied Geophysics*. 1992;**138**:611-640
- [29] Ortlepp WD. Rock Fracture and Rockbursts. Johannesburg: The South African Institute of Mining and Metallurgy; 1997
- [30] Tarasov B. Fan-hinged shear, online video, 19 July, viewed 6 December 2016. 2016. Available from: [https://www.youtube.com/watch?v=\\_-AUzCEw35M&feature=youtu.be](https://www.youtube.com/watch?v=_-AUzCEw35M&feature=youtu.be)
- [31] Lu X, Lapusta N, Rosakis AJ. Pulse-like and crack-like ruptures in experiments mimicking crustal earthquakes. *Proceedings of the National Academy of Science USA*. 2007;**104**:18931-18936
- [32] Lu X, Rosakis AJ, Lapusta N. Rupture modes in laboratory earthquakes: Effect of fault prestress and nucleation condition. *Journal of Geophysical Research*. 2010, 2010;**115**:B12302. DOI: 10.1029/2009JB006833
- [33] Segal P, Pollard DD. Mechanics of discontinuous faulting. *Journal of Geophysical Research*. 1980;**85**:4337-4350
- [34] Sibson RH. Fault zone models, heat flow, and the depth distribution of earthquakes in the continental crust of the United States. *Bulletin of the Seismological Society of America*. 1982;**72**:151-163
- [35] Tarasov BG. Fan-structure shear rupture mechanism as a source of shear rupture rockbursts. *Journal of the Southern African Institute of Mining and Metallurgy*. 2014;**114**(10):773-784
- [36] Gay NC, Ortlepp WD. Anatomy of a mining-induced fault zone. *Geological Society of America Bulletin*. 1979;**90**:47-58
- [37] McGarr A, Pollard D, Gay NC, Ortlepp WD. Observations and analysis of structures in exhumed mine-induced faults. *U.S. Geological Survey Open File Report*. 1979;**79-1**(239):101-120

- [38] Otsuki K, Dilov T. Evolution of hierarchical self-similar geometry of experimental fault zones: Implications for seismic nucleation and earthquake size. *Journal of Geophysical Research*. 2005;**110**. DOI: B03303, 10.1029/204JB003359
- [39] <http://www.geologyin.com/2018/06/slow-earthquakes-on-san-andreas-fault.html>
- [40] Chris R. Tectonics of the M7 earthquake near Christchurch. New Zealand; 2010. Available from: <http://all-geo.org/highlyallochthonous/2010/09/tectonics-of-the-m7-earthquake-near-christchurch-new-zealand/>
- [41] Temblor. Temblor. 2017. Available from: <http://www.temblor.net>
- [42] Tarasov BG. Depth distribution of lithospheric strength determined by the self-unbalancing shear rupture mechanism. In: *Proceedings of the International Symposium, Rock Mechanics for Resources, Energy and Environment (Eurock)*, Wroclaw, Poland. 2013. pp. 165-170
- [43] Tarasov BG, Guzev MA, Sadovskii VM, Cassidy MJ. Modelling the mechanical structure of extreme shear ruptures with friction approaching zero generated in brittle materials. *International Journal of Fracture*. 2017. DOI: 10.1007/s10704-017-0223-1
- [44] Tarasov BG, Guzev MA. New insight into the nature of size dependence and the lower limit of rock strength. In: Malovichko AD, editor. *Proceedings 8th International Symposium on Rockbursts and Seismicity in Mines*. Russia: St-Petersburg; 2013. pp. 31-40
- [45] Tarasov BG, Guzev MA. Mathematical model of fan-head shear rupture mechanism. *Key Engineering Materials*. 2014;**592-593**:121-124. DOI: 10.4028/www.scientific.net/KEM.592-593.121
- [46] Tarasov BG, Sadovskii VM, Sadovskaya OB. Analizis of fan waves in a laboratory model simulating the propagation of shear ruptures in rocks. *Computational Mechanics of Solids*. 2016;**9**(1):38-51. DOI: 10.7242/1999-6691/2016.9.1.4